Eur. Phys. J. A **14**, 317–348 (2002)
DOI 10.1140/epja/i2002-10011-3

THE EUROPEAN PHYSICAL JOURNAL A

Evolution of shapes in ^{59}Cu

C. Andreoiu[1,a], D. Rudolph[1], I. Ragnarsson[2], C. Fahlander[1], R.A.E. Austin[3], M.P. Carpenter[4], R.M. Clark[5], J. Ekman[1], R.V.F. Janssens[4], T.L. Khoo[4], F.G. Kondev[4,b], T. Lauritsen[4], T. Rodinger[3], D.G. Sarantites[6], D. Seweryniak[4], T. Steinhardt[7], C.E. Svensson[5,c], O. Thelen[7], and J.C. Waddington[3]

[1] Department of Physics, Lund University, S-22100 Lund, Sweden
[2] Department of Mathematical Physics, Lund Institute of Technology, S-22100 Lund, Sweden
[3] Department of Physics and Astronomy, McMaster University, Hamilton, Ontario, Canada L8S 4M1
[4] Physics Division, Argonne National Laboratory, Argonne, IL 60439, USA
[5] Nuclear Science Division, Lawrence Berkeley National Laboratory, Berkeley, CA 94720, USA
[6] Chemistry Department, Washington University, St. Louis, MO 63130, USA
[7] Institut für Kernphysik, Universität zu Köln, D-50937 Köln, Germany

Received: 15 February 2002
Communicated by D. Schwalm

Abstract. High-spin states in ^{59}Cu were populated using the fusion-evaporation reaction ^{28}Si + ^{40}Ca at a beam energy of 122 MeV. The Gammasphere Ge-detector array in conjunction with the 4π charged-particle detector array Microball allowed for the detection of γ-rays in coincidence with evaporated light particles. The resulting extensive high-spin decay scheme of ^{59}Cu is presented, which comprises more than 320 γ-ray transitions connecting about 150 excited states. Their spins and parities have been assigned via directional correlations of γ-rays emitted from oriented states. Average quadrupole moments of rotational bands have been determined from the analysis of residual Doppler shifts. Shell model calculations in the fp shell are invoked to study some of the low-spin states, while the experimental characteristics of the rotational bands are analyzed in the configuration-dependent cranked Nilsson-Strutinsky (CNS) approach.

PACS. 21.60.Cs Shell model – 23.20.Lv Gamma transitions and level energies – 23.20.En Angular distribution and correlation measurements – 27.50.+e $59 \leq A \leq 89$

1 Introduction

In recent years the study of nuclei in the vicinity of ^{56}Ni has revealed many exciting nuclear-structure phenomena. ^{56}Ni has an equal number of protons and neutrons ($N = Z = 28$). It is regarded as a doubly magic spherical nucleus at low spin and excitation energies due to the shell gap at particle number 28, which separates the $1f_{7/2}$ shell from the $2p_{3/2}$, $1f_{5/2}$ and $2p_{1/2}$ shells in the upper fp shell. Hence, ^{56}Ni is the natural core for shell model calculations in the mass $A \approx 60$ region.

An interesting feature in the $A \approx 60$ region is the occurrence of deformed and superdeformed bands at relatively moderate spins ($I \sim 10\ \hbar$) and excitation energies ($E_x \sim 10$ MeV). Following the first discovery of a superdeformed band in ^{62}Zn [1], well- and superdeformed bands were observed in the $N = Z$ nuclei ^{56}Ni [2], ^{58}Cu [3], and ^{60}Zn [4], as well as in the $N = Z + 1$ nuclei ^{59}Cu [5] and ^{61}Zn [6]. The configurations of the yrast bands have the leading component $f_{7/2}^{-4} \otimes (fp)^4 \otimes g_{9/2}^{A-56}$, where $A - 56$ is the number of nucleons in excess of ^{56}Ni. The comparison of several collective bands led to the conclusion that their quadrupole deformations scale with the number of $g_{9/2}$ particles involved in the configuration.

In contrast to other mass regions, where states in the second minimum of the nuclear potential have been identified, almost all rotational bands in the mass $A \approx 60$ region could be connected with the normal deformed, mostly spherical states in the first minimum of the nuclear potential. The "doubly magic" superdeformed band in ^{60}Zn has been linked through stretched $E2$ transitions, which allowed the firm assignment of the spin and parity of the band [4]. Recently, two superdeformed bands have been firmly linked to the spherical states in ^{59}Cu, and their band-head spins and parities established to $25/2^+$ and $23/2^-$, respectively [5,7].

[a] *Present address*: Oliver Lodge Laboratory, University of Liverpool, P.O. Box 147, Liverpool L69 3BX, UK; e-mail: ca@ns.ph.liv.ac.uk
[b] *Present address*: Technology Development Division, Argonne National Laboratory, IL 60439, USA.
[c] *Present address*: Department of Physics, University of Guelph, Guelph, Ontario, Canada N1G 2W1.

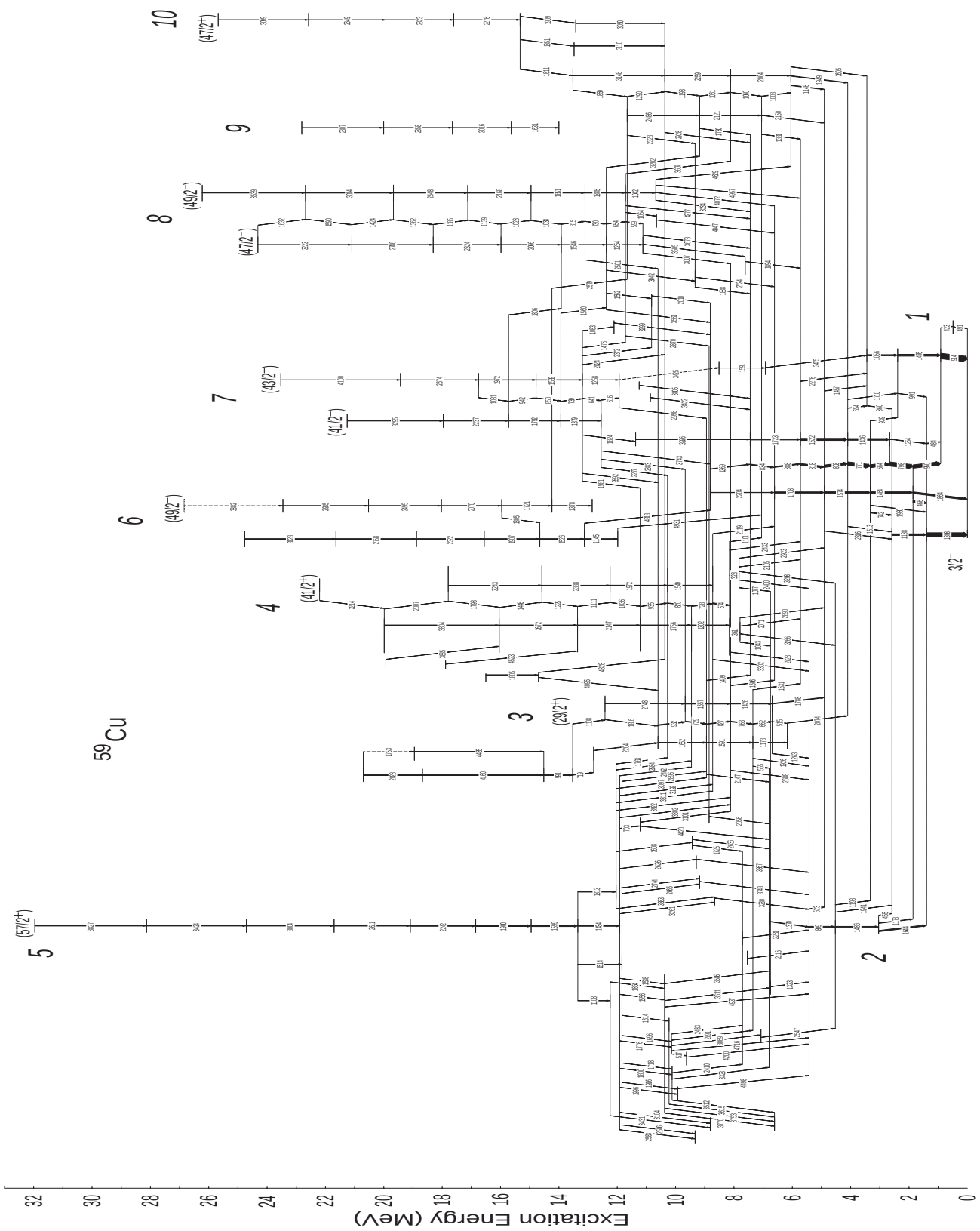

Fig. 1. Proposed high-spin level scheme of ^{59}Cu. Due to the complexity of the level scheme, spins, parities, and energies of the excited states are missing except for the ground state and the topmost levels in each band. The structures are labelled with numbers from 1 to 10. Detailed decay schemes of each structure are presented in sect. 3.

Moreover, the fact that many of the bands relate to $N = Z$ nuclei provides the opportunity to investigate possible effects of isoscalar pair correlations on the rotational behaviour [5,6]. Band termination in normally deformed rotational bands has also been successfully investigated in the mass $A \approx 60$ region. A textbook example is provided by ^{62}Zn [8]. Even some of the superdeformed bands have been followed almost up to the point of termination. For example, in ^{59}Cu the spin of the last observed state in the yrast superdeformed band is $I^{\pi} = (57/2^{+})$, which is only $4\hbar$ or two $E2$ transitions away from the maximum spin, $I_{\max} = 65/2\hbar$, which can be created from the seven valence particles and four holes involved in the band configuration [5].

The observation of prompt discrete proton and α-particle decay from superdeformed bands into spherical states of the daughter nuclei denotes the most exciting and surprising result discovered in the $A \approx 60$ region. The new decay mode has first been seen in ^{58}Cu [3], followed by a similar observation in ^{56}Ni [2], and by *two* prompt proton decays from bands in ^{59}Cu [7]. In fact, a recent dedicated experiment at Gammasphere has revealed *five* prompt proton decays from well- and superdeformed bands in ^{59}Cu [9]. Prompt α-particle decay has been identified in ^{58}Ni [10].

The present paper may be viewed as a "complete" high-spin spectroscopic study of ^{59}Cu, in which all of the afore mentioned phenomena are comprised. The following section briefly describes the experiment and applied analysis techniques. In sect. 3 the extensive level scheme is going to be discussed in some detail. Section 4 provides an interpretation of the low-lying negative-parity states in the framework of the spherical shell model and an analysis of the rotational structures in the configuration-dependent cranked Nilsson-Strutinsky (CNS) approach.

2 Experimental procedure and analysis

The experiment was performed at the Argonne National Laboratory. The heavy-ion fusion-evaporation reaction $^{28}\mathrm{Si} + ^{40}\mathrm{Ca}$ was used at a beam energy of 122 MeV. High-spin states in the residual nucleus ^{59}Cu were populated via the evaporation of two α-particles and one proton ($2\alpha 1p$ channel) from the compound nucleus ^{68}Se. An experimental relative cross-section of $\sigma_{\mathrm{rel}} \approx 6\%$ can be estimated. The 0.5 mg/cm^2 thin ^{40}Ca target was enriched to 99.975%. It was sandwiched between two thin layers of Au to prevent oxidation. The experimental set-up consisted of the Gammasphere array [11], at that time comprising 101 Ge-detectors. The array was operated in combination with the 4π charged-particle detector array Microball [12]. The heavimet collimators were removed from the Gammasphere detectors to provide γ-ray multiplicity and sum energy measurements [13] as well as additional selectivity by total energy conservation requirements (TE-gating) [14]. The event trigger required the detection of at least four Compton-suppressed γ-rays. The charged particles were detected and identified in the Microball using pulse-shape discrimination techniques [12]. Based on the charged-particle energies and directions detected in Microball, the momenta of the recoiling residual nuclei can be determined for each event. This allowed for a more accurate Doppler-shift correction of the γ-ray energies, leading to a significantly improved energy resolution. The events were sorted off-line into various E_γ projections, E_γ-E_γ matrices, and E_γ-E_γ-E_γ cubes subject to appropriate evaporated-particle conditions. Their examination employed the Radware software package [15] and the spectrum-analysis code Tv [16].

The main result of the present charged-particle- and TE-gated $\gamma\gamma$- and $\gamma\gamma\gamma$-coincidence analysis is the rich high-spin excitation scheme of ^{59}Cu, which is shown schematically in fig. 1. It is based on coincidence relations, intensity balances, and summed energy relations. Contaminations from higher fold charged-particle channels, in particular from the $2\alpha 2p$ channel corresponding to ^{58}Ni, can be easily eliminated by careful subtraction of, for example, $2\alpha 2p$-gated spectra from the corresponding $2\alpha 1p$-gated spectra. Ten different structures are labelled in fig. 1, which will be discussed one by one in the next section. The level energies, the corresponding depopulating γ-rays, their relative intensities, their angular-correlation ratios, and resulting spin-parity assignments are summarized in table 1.

The assignment of the multipolarities to γ-ray transitions is based on their directional correlations (DCO-ratios) following the emission from oriented states. The Ge-detectors in Gammasphere were grouped into three "pseudo"-rings labelled "30°" (25 detectors at 31.7°, 37.4°, 142.6°, 148.3°, and 162.7°), "53°" (30 detectors at 50.1°, 58.3°, 121.7° and 129.9°) and "83°" (28 detectors at 79.2°, 80.7°, 90.0°, 99.3°, and 100.8°), respectively. This procedure was found to provide a good compromise between statistics and significance.

For example, the DCO-ratios R_{DCO}(30-83) are defined as [18]

$$R_{\mathrm{DCO}}(30\text{-}83) = \frac{I(\gamma_1 \text{ at } 30^\circ;\ \text{gated with } \gamma_2 \text{ at } 83^\circ)}{I(\gamma_1 \text{ at } 83^\circ;\ \text{gated with } \gamma_2 \text{ at } 30^\circ)}, \quad (1)$$

where the intensities I were extracted from a $2\alpha 1p$- and TE-gated γ-γ matrix with γ-rays detected at 30° sorted on one axis and 83° on the other axis of the matrix. The DCO-ratios R_{DCO}(30-53) and R_{DCO}(53-83) are defined and determined accordingly. The DCO-ratios R_{DCO}(30-83), which could be deduced for most of the γ-ray transitions in the level scheme, are summarized in table 1. They were obtained by gating on known stretched $E2$ transitions. For stretched $\Delta I = 2$ transitions $R_{\mathrm{DCO}} = 1.0$ is expected, while pure stretched $\Delta I = 1$ transitions should reveal $R_{\mathrm{DCO}} \approx 0.6$. Deviations from the latter may arise from quadrupole admixtures, *i.e.*, non-zero $\delta(E2/M1)$ mixing ratios ($M2$ admixtures into $E1$ dipoles are considered unlikely). Non-stretched $\Delta I = 0$ transitions typically result in $R_{\mathrm{DCO}} \approx 1.0$, but this value also depends on the multipole mixing ratio.

The investigation of three DCO-ratios for a given transition allowed for an evaluation of $\delta(E2/M1)$ mixing ratios for many of the $\Delta I = 0$ and stretched $\Delta I = 1$

Table 1. The energies of excited states in ^{59}Cu, the transition energies and relative intensities of the γ-rays placed in the level scheme, angular-correlation ratios, and the spins and parities of the initial and final states of the γ-rays. The last column indicates into which structure (cf. fig. 1) the states are grouped.

E_x (keV)	E_γ (keV)	$I_{\rm rel}$ (%)	$R_{30\text{-}83}$	Mult. ass.	$I_{\rm i}^\pi$ ($\hbar$)	$I_{\rm f}^\pi$ ($\hbar$)	Structure no.
491(1)	491.3(3)	0.7(2)		$E2/M1$	$1/2^-$	$3/2^-$	1
914(1)	422.6(4)	0.7(2)		$E2$	$5/2^-$	$1/2^-$	1
	913.5(2)	100(3)	0.44(4)	$E2/M1$	$5/2^-$	$3/2^-$	1
1398(1)	484.3(1)	13.1(4)	0.50(8)	$E2/M1$	$7/2^-$	$5/2^-$	1
	1398.4(3)	80(2)	0.95(7)	$E2$	$7/2^-$	$3/2^-$	1
1864(1)	465.8(1)	36(1)	0.94(7)	$\Delta I = 0$	$7/2^-$	$7/2^-$	1
	950.5(2)	61(2)	0.65(5)	$E2/M1$	$7/2^-$	$5/2^-$	1
	1864.2(4)	31(1)	1.06(9)	$E2$	$7/2^-$	$3/2^-$	1
2389(1)	990.8(2)	4.0(3)	0.48(4)	$E2/M1$	$9/2^-$	$7/2^-$	1
	1476.4(3)	34(1)	0.95(5)	$E2$	$9/2^-$	$5/2^-$	1
2586(1)	1187.5(3)	31(2)	0.97(8)	$E2$	$11/2^-$	$7/2^-$	1
2663(1)	196.3(2)	1.6(4)		$\Delta I = 0$	$9/2^-$	$9/2^-$	1
	798.5(2)	76(2)	0.90(5)	$E2/M1$	$9/2^-$	$7/2^-$	1
	1264.4(3)	5.4(4)	1.29(12)	$E2/M1$	$9/2^-$	$7/2^-$	1
3041(1)	455.4(1)	0.4(1)	0.73(9)	$E1$	$9/2^+$	$11/2^-$	2
	1177.5(2)	8.5(4)	0.59(4)	$E1$	$9/2^+$	$7/2^-$	2
	1643.5(3)	22(1)	0.58(3)	$E1$	$9/2^+$	$7/2^-$	2
3328(1)	664.5(2)	54(2)	0.76(4)	$E2/M1$	$11/2^-$	$9/2^-$	1
	741.7(2)[a]	14(1)	1.00(9)	$\Delta I = 0$	$11/2^-$	$11/2^-$	1
	938.9(4)[a,b]	2.0(3)	0.48(13)	$E2/M1$	$11/2^-$	$9/2^-$	1
	1464.4(4)	26(1)	1.06(6)	$E2$	$11/2^-$	$7/2^-$	1
	1930.3(4)	7.2(4)	0.94(6)	$E2$	$11/2^-$	$7/2^-$	1
3445(1)	860.1(2)	4.0(5)	0.25(4)	$E2/M1$	$13/2^-$	$11/2^-$	1
	1056.3(3)	21(1)	1.07(9)	$E2$	$13/2^-$	$9/2^-$	1
4099(1)	653.5(1)[c]	6.3(7)	0.95(6)	$\Delta I = 0$	$13/2^-$	$13/2^-$	1
	770.7(2)	64(2)	0.78(4)	$E2/M1$	$13/2^-$	$11/2^-$	1
	1435.7(3)	32(3)	1.02(6)	$E2$	$13/2^-$	$9/2^-$	1
	1513.0(4)	2.7(4)		$E2/M1$	$13/2^-$	$11/2^-$	1
	1709.6(5)[c]	1.4(3)		$E2$	$13/2^-$	$9/2^-$	1
4526(1)	1198.2(2)	2.3(3)	0.65(14)	$E1$	$13/2^+$	$11/2^-$	1
	1485.5(3)	20(1)	0.95(6)	$E2$	$13/2^+$	$9/2^+$	1
	1941.2(4)	1.6(4)	0.40(16)	$E1$	$13/2^+$	$11/2^-$	1
4902(1)	802.7(2)	43(1)	0.82(6)	$E2/M1$	$15/2^-$	$13/2^-$	1
	1457.3(3)[a]	5.4(4)	0.38(3)	$E2/M1$	$15/2^-$	$13/2^-$	1
	1574.3(3)	37(2)	1.15(7)	$E2$	$15/2^-$	$11/2^-$	1
	2315.5(6)[b]	7.0(8)	1.08(11)	$E2$	$15/2^-$	$11/2^-$	1
5425(1)	523.0(1)	9.0(3)		$E1$	$17/2^+$	$15/2^-$	2
	898.7(2)	22(1)	1.04(6)	$E2$	$17/2^+$	$13/2^+$	2
5720(1)	818.1(2)	31(1)	0.74(4)	$E2/M1$	$17/2^-$	$15/2^-$	1
	1621.6(3)	40(2)	1.07(7)	$E2$	$17/2^-$	$13/2^-$	1
	2275.8(5)[c]	7.0(5)	1.25(9)	$E2$	$17/2^-$	$13/2^-$	1
6048(2)	1145.5(2)	10.4(6)	0.92(6)	$E2/M1$	$17/2^-$	$15/2^-$	10
	1949.1(4)	9.7(5)	0.98(7)	$E2$	$17/2^-$	$13/2^-$	10
	2605(1)	2.2(4)	0.97(11)	$E2$	$17/2^-$	$13/2^-$	10
6173(2)	2074.2(4)[a]	5.0(5)	0.57(9)	$E1$	$15/2^+$	$13/2^-$	3
6609(2)	888.1(2)	16.0(5)	0.75(5)	$E2/M1$	$19/2^-$	$17/2^-$	1
	1707.4(3)	23(1)	1.12(7)	$E2$	$19/2^-$	$15/2^-$	1
6689(2)	515.4(2)	1.9(3)		$E2/M1$	$17/2^+$	$15/2^+$	3
	1263.4(3)	2.1(3)	0.86(14)	$\Delta I = 0$	$17/2^+$	$17/2^+$	3
	1788.1(4)	12(1)	0.53(5)	$E1$	$17/2^+$	$15/2^-$	3
6748(2)	1322.9(4)	1.8(3)	1.33(33)	$(\Delta I = 0)$	$(17/2^+)$	$17/2^+$	5
6795(2)	1370.1(3)	9.5(6)	0.60(4)	$E2/M1$	$19/2^+$	$17/2^+$	1
6920(3)	3475(3)	0.9(1)	0.90(18)	$(E2)$	$(17/2^-)$	$13/2^-$	1

Table 1. Continued.

E_x (keV)	E_γ (keV)	$I_{\rm rel}$ (%)	$R_{30\text{-}83}$	Mult. ass.	$I_{\rm i}^{\pi}$ ($\hbar$)	$I_{\rm f}^{\pi}$ ($\hbar$)	Structure no.
7051(2)	1003.1(2)[a]	8.3(6)	1.32(7)	$E2/M1$	$19/2^-$	$17/2^-$	10
	1331.2(3)	1.9(3)	0.49(11)	$E2/M1$	$19/2^-$	$17/2^-$	10
	2149.6(4)	1.7(3)	1.03(21)	$E2$	$19/2^-$	$15/2^-$	10
7073(4)	2547(1)	0.8(2)	1.19(17)	$E2$	$17/2^+$	$13/2^+$	5
7351(2)	555.3(2)	0.7(2)	0.99(14)	$\Delta I=0$	$19/2^+$	$19/2^+$	3
	662.2(2)[c]	7.0(8)	0.65(4)	$E2/M1$	$19/2^+$	$17/2^+$	3
	1177.9(3)	1.0(3)	0.89(14)	$E2$	$19/2^+$	$15/2^+$	3
	1630.7(3)	10(1)	0.56(4)	$E1$	$19/2^+$	$17/2^-$	3
	1925.8(7)	2.0(3)	0.48(8)	$E2/M1$	$19/2^+$	$17/2^+$	3
7443(2)	833.7(2)	15(1)	0.78(5)	$E2/M1$	$21/2^-$	$19/2^-$	1
	1723.3(3)	20(1)	0.94(5)	$E2$	$21/2^-$	$17/2^-$	1
7541(3)	2116(2)	0.3(1)				$17/2^+$	5
7615(4)	1894(1)[c]	2.3(5)		$E2$	$21/2^-$	$17/2^-$	1
7707(3)	2281.1(5)[c]	2.4(8)	0.85(15)	$E2/M1$	$19/2^+$	$17/2^+$	5
7792(2)	1043(1)[b]	0.2(1)		$(\Delta I=0)$	$17/2^+$	$(17/2^+)$	4
	2071(1)	0.7(3)		$\Delta I=0$	$17/2^+$	$17/2^-$	4
	2890(1)	1.9(5)	0.62(8)	$E1$	$17/2^+$	$15/2^-$	4
	3266(2)	0.2(1)		$E2$	$17/2^+$	$13/2^+$	4
7825(2)	1077(1)[b]	<0.1		$(\Delta I=0)$	$17/2^+$	$(17/2^+)$	4
	2105(1)	0.5(2)		$\Delta I=0$	$17/2^+$	$17/2^-$	4
	2400(1)	0.4(1)		$\Delta I=0$	$17/2^+$	$17/2^+$	4
	2923(1)	1.8(2)	0.47(14)	$E1$	$17/2^+$	$15/2^-$	4
	3298(2)	0.3(1)		$E2$	$17/2^+$	$13/2^+$	4
8112(3)	1060(1)	2.0(5)	0.83(6)[c]	$E2/M1$	$21/2^-$	$19/2^-$	10
	2064(1)[b]	6.9(5)	1.03(7)	$E2$	$21/2^-$	$17/2^-$	10
8114(2)	762.9(2)	12(1)	0.61(6)	$E2/M1$	$21/2^+$	$19/2^+$	3
	1426.0(3)	8.0(8)	0.90(11)	$E2$	$21/2^+$	$17/2^+$	3
	1505.5(3)	5.0(2)	0.47(6)	$E1$	$21/2^+$	$19/2^-$	3
	2688(1)[b]	1.6(3)		$E2$	$21/2^+$	$17/2^+$	3
8153(2)	327.9(1)	6.3(2)	0.65(11)	$E2/M1$	$19/2^+$	$17/2^+$	4
	360.9(1)	4.8(2)	0.61(10)	$E2/M1$	$19/2^+$	$17/2^+$	4
	1101.1(4)[b]	0.5(2)		$\Delta I=0$	$19/2^+$	$19/2^-$	4
	2432.8(6)	5.1(4)	0.46(6)	$E1$	$19/2^+$	$17/2^-$	4
	2728(1)	1.3(2)	1.20(13)	$E2/M1$	$19/2^+$	$17/2^+$	4
8511(3)	1591(1)[c]	0.4(2)	1.00(12)	$(E2)$	$(21/2^-)$	$(17/2^-)$	1
8656(5)	3230(2)	2.4(3)	1.07(12)	$E2$	$21/2^+$	$17/2^+$	5
8727(2)	574.1(1)	17.3(5)	0.71(7)	$E2/M1$	$21/2^+$	$19/2^+$	4
	2118.7(7)	2.1(5)	0.55(15)	$E1$	$21/2^+$	$19/2^-$	4
	3302(1)	2.1(2)	1.10(19)	$E2$	$21/2^+$	$17/2^+$	4
8812(2)	1368.7(3)	9.0(5)	0.78(9)	$E2/M1$	$23/2^-$	$21/2^-$	1
	2204.0(4)	4.5(4)	0.92(8)	$E2$	$23/2^-$	$19/2^-$	1
8851(3)	2055.5(4)[d]	1.9(5)	0.65(26)	$E1$	$21/2^-$	$19/2^+$	8
8942(2)	827.4(2)	10(1)	0.75(5)	$E2/M1$	$23/2^+$	$21/2^+$	3
	1499.1(10)	8.0(2)	0.63(6)	$E1$	$23/2^+$	$21/2^-$	3
	1591.1(3)	10(1)	1.01(8)	$E2$	$23/2^+$	$19/2^+$	3
	2147(1)	0.6(2)	0.82(11)	$E2$	$23/2^+$	$19/2^+$	3
9173(3)	1061(1)[c]	1.5(5)	0.83(6)[c]	$E2/M1$	$23/2^-$	$21/2^-$	10
	1730(1)[a,c]	1.4(3)	0.80(13)	$E2/M1$	$23/2^-$	$21/2^-$	10
	2121.4(8)	5.0(9)	1.27(14)	$E2$	$23/2^-$	$19/2^-$	10
9173(5)	3748(2)	0.6(1)	1.07(15)	$E2$	$21/2^+$	$17/2^+$	5
9292(8)	3867(2)	0.6(2)	0.87(13)	$E2$	$21/2^+$	$17/2^+$	5
9332(2)	1888.5(4)[c]	5.0(5)	[c]	$E2/M1$	$23/2^-$	$21/2^-$	8
	2724(1)	0.9(2)		$E2$	$23/2^-$	$19/2^-$	8
9431(4)	1725(1)[c]	0.4(1)	0.77(18)	$E2/M1$	$21/2^+$	$19/2^+$	5
	2636(1)	1.5(3)	0.63(11)	$E2/M1$	$21/2^+$	$19/2^+$	5

Table 1. Continued.

E_x (keV)	E_γ (keV)	$I_{\rm rel}$ (%)	$R_{30\text{-}83}$	Mult. ass.	$I_{\rm i}^{\pi}$ ($\hbar$)	$I_{\rm f}^{\pi}$ ($\hbar$)	Structure no.
9455(2)	727.5(1)[c]	13(1)	0.81(5)	$E2/M1$	$23/2^+$	$21/2^+$	4
	1302.1(3)[c]	4.0(5)	1.31(16)	$E2$	$23/2^+$	$19/2^+$	4
9624(6)	4200(3)	0.3(1)			$21/2^+$	$17/2^+$	5
9671(2)	729.4(1)[c]	11(1)	0.80(7)	$E2/M1$	$25/2^+$	$23/2^+$	3
	1557.1(3)	9(1)	0.99(7)	$E2$	$25/2^+$	$21/2^+$	3
9922(5)	4498(3)	0.3(1)		$E2$	$21/2^+$	$17/2^+$	5
10119(3)	2410(2)	0.2(1)		$E2/M1$	$21/2^+$	$19/2^+$	5
	3323(2)	0.2(1)		$E2/M1$	$21/2^+$	$19/2^+$	5
	3512(2)	0.2(1)		$E1$	$21/2^+$	$19/2^-$	5
10141(2)	517(1)	< 0.1			$21/2^+$	$21/2^+$	5
	2433(1)	0.3(1)	0.38(6)	$E2/M1$	$21/2^+$	$19/2^+$	5
	2791(2)	< 0.1		$E2/M1$	$21/2^+$	$19/2^+$	5
	3069(1)	0.3(1)		$E2$	$21/2^+$	$17/2^+$	5
	4716(2)	0.8(2)	0.95(13)	$E2$	$21/2^+$	$17/2^+$	5
10224(9)	3615(3)	0.4(1)		$E1$	$21/2^+$	$19/2^-$	5
10276(2)	819.8(2)[c]	6.6(4)	0.73(6)	$E2/M1$	$25/2^+$	$23/2^+$	4
	1548.8(4)	5.0(7)	1.18(27)	$E2$	$25/2^+$	$21/2^+$	4
10361(5)	3611(3)	< 0.1		$(E2)$	$21/2^+$	$(17/2^+)$	5
	3753(2)[c]	0.8(5)	[c]	$E1$	$21/2^+$	$19/2^-$	5
	4937(4)	0.3(1)	0.93(23)	$E2$	$21/2^+$	$17/2^+$	5
10370(3)	1197.8(6)	0.7(1)	0.61(24)[c]	$E2/M1$	$25/2^-$	$23/2^-$	10
	2259(1)	4.0(9)	1.01(18)	$E2$	$25/2^-$	$21/2^-$	10
	2928(1)	0.8(3)	1.01(31)	$E2$	$25/2^-$	$21/2^-$	10
10379(4)	3586(3)	0.3(1)		$E2/M1$	$21/2^+$	$19/2^+$	5
	3770(2)	0.5(2)		$E1$	$21/2^+$	$19/2^-$	5
10603(2)	932.1(2)	14(1)	0.89(6)	$E2/M1$	$27/2^+$	$25/2^+$	3
	1662.0(3)	8.0(6)	1.02(7)	$E2$	$27/2^+$	$23/2^+$	3
10656(4)	4047(4)	0.4(1)			$21/2^-$	$19/2^-$	8
10677(5)	3234(2)	0.3(1)	1.02(15)	$\Delta I = 0$	$21/2^-$	$21/2^-$	8
	4072(4)	< 0.1		$E2/M1$	$21/2^-$	$19/2^-$	8
	4629(3)	0.2(1)		$E2$	$21/2^-$	$17/2^-$	8
	4957(4)	0.2(1)	1.09(45)	$E2$	$21/2^-$	$17/2^-$	8
10822(3)	2010.4(4)	2.0(7)	1.16(26)	$(E2/M1)$	$(25/2^-)$	$23/2^-$	8
10865(4)	3422(3)	1.0(3)	0.61(12)	$E2/M1$	$23/2^-$	$21/2^-$	1
11121(3)	3007(2)	2.0(3)	0.57(6)	$E1$	$23/2^-$	$21/2^+$	8
	3505(2)	0.5(1)	0.39(14)	$E2/M1$	$23/2^-$	$21/2^-$	8
	3678(2)	1.7(2)	0.19(5)	$E2/M1$	$23/2^-$	$21/2^-$	8
11211(2)	935.0(2)[c]	4.1(3)	[c]	$E2/M1$	$27/2^+$	$25/2^+$	4
	1756.3(3)	5.4(3)	1.14(11)	$E2$	$27/2^+$	$23/2^+$	4
11215(4)	3101(2)	< 0.1		$(E2/M1)$	$(23/2^+)$	$21/2^+$	5
	4420(3)	< 0.1		$(E2)$	$(23/2^+)$	$19/2^+$	5
11248(4)	3805(3)	0.9(2)	0.62(16)	$\Delta I = 1$	23/2	$21/2^-$	1
11369(3)	3926(3)	0.9(5)	0.85(21)	$E2$	$25/2^-$	$21/2^-$	1
11660(4)	1290(1)[b]	0.4(3)		$E2/M1$	$27/2^-$	$25/2^-$	10
	2328(1)	0.8(3)	1.24(18)	$E2$	$27/2^-$	$23/2^-$	10
	2486(1)	1.1(5)	1.00(23)	$E2$	$27/2^-$	$23/2^-$	10
11719(3)	598.8(1)	4.0(3)	0.47(4)	$E2/M1$	$25/2^-$	$23/2^-$	8
	1042.4(9)	1.4(2)	1.11(22)	$E2$	$25/2^-$	$21/2^-$	8
	1064(2)	0.2(1)			$25/2^-$	$21/2^-$	8
	2870(1)	0.8(2)	1.04(22)	$E2$	$25/2^-$	$21/2^-$	8
	3607(3)[b]	0.3(1)			$25/2^-$	$21/2^-$	8
	4277(3)	2.0(2)	0.94(11)	$E2$	$25/2^-$	$21/2^-$	8

Table 1. Continued.

E_x (keV)	E_γ (keV)	$I_{\rm rel}$ (%)	$R_{30\text{-}83}$	Mult. ass.	$I_{\rm i}^\pi$ ($\hbar$)	$I_{\rm f}^\pi$ ($\hbar$)	Structure no.
11838(3)	1614(1)	0.8(2)	1.30(15)	$E2$	$25/2^+$	$21/2^+$	5
	1696(2)	0.5(1)		$E2$	$25/2^+$	$21/2^+$	5
	1718(1)[c]	0.5(1)		$E2$	$25/2^+$	$21/2^+$	5
	1916(1)	0.6(1)		$E2$	$25/2^+$	$21/2^+$	5
	2506(1)	0.4(1)	0.73(21)	$E1$	$25/2^+$	$23/2^-$	5
	2665(2)[b,c]	< 0.1		$E2$	$25/2^+$	$21/2^+$	5
	2896(2)	0.8(2)	0.48(19)	$E2/M1$	$25/2^+$	$23/2^+$	5
11917(3)	703(1)	0.2(1)		$(E2/M1)$	$25/2^+$	$(23/2^+)$	5
	1538(1)	1.1(2)		$E2$	$25/2^+$	$21/2^+$	5
	1556(1)[c]	3.1(3)	1.25(10)	$E2$	$25/2^+$	$21/2^+$	5
	1776(1)	2.3(1)	0.92(25)	$E2$	$25/2^+$	$21/2^+$	5
	1800(1)	0.5(1)		$E2$	$25/2^+$	$21/2^+$	5
	1996(2)	0.3(1)		$E2$	$25/2^+$	$21/2^+$	5
	2462(1)	2.4(4)	0.69(8)	$E2/M1$	$25/2^+$	$23/2^+$	5
	2583(2)	1.4(4)	0.50(5)	$E1$	$25/2^+$	$23/2^-$	5
	2626(2)	0.2(1)		$E2$	$25/2^+$	$21/2^+$	5
	2744(2)	0.4(1)		$E2$	$25/2^+$	$21/2^+$	5
	3104(2)	0.8(2)	0.40(9)	$E1$	$25/2^+$	$23/2^-$	5
	3192(2)	0.2(1)		$E2$	$25/2^+$	$21/2^+$	5
	3261(2)	1.0(3)	0.87(15)	$E2$	$25/2^+$	$21/2^+$	5
	3802(2)	0.8(3)		$E2$	$25/2^+$	$21/2^+$	5
11936(3)	2998(2)			$E1$	$25/2^-$	$23/2^+$	7
	3425(3)	< 0.1		$E2$	$25/2^-$	$(21/2^-)$	7
11982(4)	4931(2)	< 0.1		$E2$	$23/2^-$	$19/2^-$	6
12039(3)	1763(1)	0.4(2)		$\Delta I = 0$	$25/2^+$	$25/2^+$	5
	2584(1)	1.0(3)	0.76(10)	$E2/M1$	$25/2^+$	$23/2^+$	5
	2608(1)	0.5(3)		$E2$	$25/2^+$	$21/2^+$	5
	3097(2)	0.2(1)		$E2/M1$	$25/2^+$	$23/2^+$	5
	3311(2)	0.2(1)		$E2$	$25/2^+$	$21/2^+$	5
	3383(2)[b]	< 0.1		$E2$	$25/2^+$	$21/2^+$	5
	3922(2)	1.4(3)	1.11(10)	$E2$	$25/2^+$	$21/2^+$	5
12111(5)	3299(2)	1.2(1)	1.28(32)	$E2$	$27/2^-$	$23/2^-$	7
12243(3)	1864(1)	0.3(1)	1.05(29)	$E2$	$25/2^+$	$21/2^+$	5
	3431(2)	0.4(1)	0.64(12)	$E1$	$25/2^+$	$23/2^-$	5
12247(2)	1035.0(3)	1.9(3)	0.59(6)	$E2/M1$	$29/2^+$	$27/2^+$	4
	1971.7(4)	4.1(5)	0.93(8)	$E2$	$29/2^+$	$25/2^+$	4
12374(3)	654.0(1)	4.0(5)	0.50(4)	$E2/M1$	$27/2^-$	$25/2^-$	8
	1253.6(3)	2.9(5)	1.08(11)	$E2$	$27/2^-$	$23/2^-$	8
	1552(1)	0.4(1)	[c]		$27/2^-$	$(25/2^-)$	8
	3042(2)	1.2(3)	1.01(15)	$E2$	$27/2^-$	$23/2^-$	8
	3202(3)	1.1(6)	1.27(21)	$E2$	$27/2^-$	$23/2^-$	8
	3561(2)	2.0(5)	1.00(16)	$E2$	$27/2^-$	$23/2^-$	8
12419(2)	1815.6(4)	3.2(4)	0.88(10)	$E2/M1$	$29/2^+$	$27/2^+$	3
	2748(1)	2.0(1)		$E2$	$29/2^+$	$25/2^+$	3
12552(2)	615.8(1)	0.4(2)		$E2/M1$	$27/2^-$	$25/2^-$	7
	2277(2)	1.0(3)	0.53(9)	$E1$	$27/2^-$	$25/2^+$	7
	2883(2)[c]	0.8(3)	0.75(20)	$E1$	$27/2^-$	$25/2^+$	7
	3743(3)	< 0.1		$E2$	$27/2^-$	$23/2^-$	7
12808(2)	2204.5(4)	6.8(5)	0.55(4)	$\Delta I = 1$	29/2	$27/2^+$	3
13104(3)	730.0(1)	4.0(4)	0.51(4)	$E2/M1$	$29/2^-$	$27/2^-$	8
	1385.1(9)	4.0(1)	1.13(9)	$E2$	$29/2^-$	$25/2^-$	8
	2501(1)	1.3(2)	0.39(9)	$E1$	$29/2^-$	$27/2^+$	8
13127(5)	1145(1)	1.2(2)	1.23(19)	$E2$	$27/2^-$	$23/2^-$	6
	4313(2)	1.4(2)	0.97(11)	$E2$	$27/2^-$	$23/2^-$	6

Table 1. Continued.

E_x (keV)	E_γ (keV)	$I_{\rm rel}$ (%)	$R_{30\text{-}83}$	Mult. ass.	$I_{\rm i}^{\pi}$ ($\hbar$)	$I_{\rm f}^{\pi}$ ($\hbar$)	Structure no.
13194(2)	641.4(1)	1.5(3)	1.06(12)	$E2/M1$	$29/2^-$	$27/2^-$	7
	1083(1)	0.3(1)	0.75(10)	$E2/M1$	$29/2^-$	$27/2^-$	7
	1257.9(3)	0.6(3)	1.24(18)	$E2$	$29/2^-$	$25/2^-$	7
	1476(1)[c]	0.4(1)	[c]	$E2$	$29/2^-$	$25/2^-$	7
	1824(1)	< 0.1		$E2$	$29/2^-$	$25/2^-$	7
	1981.1(4)	1.1(3)		$E1$	$29/2^-$	$27/2^+$	7
	2372(1)	0.4(1)		$E2$	$29/2^-$	$25/2^-$	7
	2591(1)	3.0(4)	0.55(4)	$E1$	$29/2^-$	$27/2^+$	7
	2824(2)	0.8(3)	0.91(26)	$E2$	$29/2^-$	$25/2^+$	7
13351(4)	1108(1)	1.1(1)	0.89(12)	$E2$	$29/2^+$	$25/2^+$	5
	1313(1)	4.9(3)	1.03(7)	$E2$	$29/2^+$	$25/2^+$	5
	1434(1)	17(1)	1.07(7)	$E2$	$29/2^+$	$25/2^+$	5
	1514(1)	4.1(3)	0.90(6)	$E2$	$29/2^+$	$25/2^+$	5
13358(3)	1111.0(6)	1.1(2)	1.12(14)	$E2/M1$	$31/2^+$	$27/2^+$	4
	2147.1(5)	4.3(3)	1.01(13)	$E2$	$31/2^+$	$27/2^+$	4
13421(5)	3050(3)	0.8(3)	1.01(15)	$E2$	$29/2^-$	$25/2^-$	10
13479(5)	3110(3)[c]	0.4(2)	0.6(2)	$\Delta I = 1$	$27/2^{(+)}$	$25/2^-$	10
13519(5)	1858.9(20)	0.4(2)	[c]	$(E2/M1)$	$(29/2^-)$	$27/2^-$	10
	3148(3)	0.9(2)	1.3(3)	$(E2)$	$(29/2^-)$	$25/2^-$	10
13527(2)	718.6(1)	4.0(5)	0.68(5)	$E2/M1$	$31/2$	$29/2$	3
	1108.0(2)	1.8(3)	0.63(6)	$\Delta I = 1$	$31/2$	$29/2^+$	3
13918(3)	814.6(2)	2.0(1)	0.50(7)	$E2/M1$	$31/2^-$	$29/2^-$	8
	1545.6(3)	2.5(5)	1.01(10)	$E2$	$31/2^-$	$27/2^-$	8
13933(3)	739(1)[c]	0.3(1)	0.91(6)	$E2/M1$	$31/2^-$	$29/2^-$	7
	1379(1)	1.0(2)	0.99(13)	$E2$	$31/2^-$	$27/2^-$	7
	1560(1)[c]	4.5(5)	1.26(9)	$E2$	$31/2^-$	$27/2^-$	7
14237(5)	1378(1)[c]	0.6(2)	[c]	$(E2)$	$29/2^-$	$(25/2^-)$	6
	2579(2)[a,d]	0.4(1)	0.85(14)	$E2/M1$	$29/2^-$	$27/2^-$	6
14517(3)	990.8(2)	3.7(5)	0.71(7)	$E2/M1$	$33/2$	$31/2$	3
14585(3)	1225(1)[a]	0.9(2)		$E2/M1$	$33/2^+$	$31/2^+$	4
	2338.3(5)	2.2(3)	0.91(10)	$E2$	$33/2^+$	$29/2^+$	4
14653(6)	1526(1)	2.7(3)	1.16(10)	$E2$	$31/2^-$	$27/2^-$	6
14698(6)	4095(3)	0.5(1)				$27/2^+$	
	4328(3)	0.2(1)				$25/2^-$	
14782(3)	850(1)	0.8(2)	1.24(10)	$E2/M1$	$33/2^-$	$31/2^-$	7
	1588.7(3)	6.0(4)	0.98(10)	$E2$	$33/2^-$	$29/2^-$	7
14951(5)	1599.3(5)	25(1)	1.05(6)	$E2$	$33/2^+$	$29/2^+$	5
14955(4)	1038(1)[c]	2.5(5)	0.35(4)	$E2/M1$	$33/2^-$	$31/2^-$	8
	1850.9(8)	3.5(5)	1.13(13)	$E2$	$33/2^-$	$29/2^-$	8
15330(6)	1811(1)[c]	0.9(3)	0.67(7)	$\Delta I = 1$	$31/2^{(+)}$	$(29/2^-)$	10
	1851(1)[c]	< 0.1	[c]	$E2$	$31/2^{(+)}$	$27/2^{(+)}$	10
	1909(1)[c]	0.5(2)		$\Delta I = 1$	$31/2^{(+)}$	$29/2^-$	10
15724(3)	942(1)	0.6(1)	0.77(11)	$E2/M1$	$35/2^-$	$33/2^-$	7
	1791.6(4)	2.5(3)	1.04(13)	$E2$	$35/2^-$	$31/2^-$	7
	1806(1)	1.0(2)	0.88(10)	$E2$	$35/2^-$	$31/2^-$	7
15958(6)	1304.8(5)[c]	0.4(1)	0.46(8)	$E2/M1$	$33/2^-$	$31/2^-$	6
	1721(1)[c]	1.2(2)	1.06(11)	$E2$	$33/2^-$	$29/2^-$	6
15984(5)	1028(1)	2.0(8)	0.43(5)	$E2/M1$	$35/2^-$	$33/2^-$	8
	2066(1)[c]	3.8(8)	0.96(7)[c]	$E2$	$35/2^-$	$31/2^-$	8
16030(4)	1445(1)[b]	0.4(1)		$E2/M1$	$35/2^+$	$33/2^+$	4
	2672(1)[c]	1.7(3)	1.04(10)	$E2$	$35/2^+$	$31/2^+$	4
16503(7)	1805(1)	0.3(1)					
16560(7)	1907(1)	1.9(4)	1.01(8)	$E2$	$35/2^-$	$31/2^-$	6

Table 1. Continued.

E_x (keV)	E_γ (keV)	$I_{\rm rel}$ (%)	$R_{30\text{-}83}$	Mult. ass.	$I_{\rm i}^\pi$ ($\hbar$)	$I_{\rm f}^\pi$ ($\hbar$)	Structure no.
16755(4)	1031(1)[c]	0.5(1)	1.12(8)	$E2/M1$	$37/2^-$	$35/2^-$	7
	1972.4(6)[c]	5.5(1)	1.06(7)	$E2$	$37/2^-$	$33/2^-$	7
16851(6)	1899.8(6)	23(1)	1.12(6)	$E2$	$37/2^+$	$33/2^+$	5
17123(5)	1139(1)	2.0(10)	0.55(6)	$E2/M1$	$37/2^-$	$35/2^-$	8
	2168(1)	6.0(10)	1.20(11)	$E2$	$37/2^-$	$33/2^-$	8
17606(6)	2276(1)[c]	1.4(2)	1.1(2)	$E2$	$35/2^{(+)}$	$31/2^{(+)}$	10
17828(5)	1798(2)[a,c]	0.2(1)		$(E2/M1)$	$(37/2^+)$	$35/2^+$	4
	3243(2)	0.6(2)		$(E2)$	$(37/2^+)$	$33/2^+$	4
17881(5)	4523(4)	0.2(1)				$31/2^+$	4
17961(4)	2237(1)	3.5(3)	0.99(8)	$E2$	$39/2^-$	$35/2^-$	7
18028(7)	2070.1(7)[c]	1.2(2)	1.19(13)	$E2$	$37/2^-$	$33/2^-$	6
18308(6)	1185(1)[c]	1.7(5)	0.70(6)	$E2/M1$	$39/2^-$	$37/2^-$	8
	2324(1)	3.4(3)	1.10(8)	$E2$	$39/2^-$	$35/2^-$	8
18677(6)	4160(4)	0.2(1)				$33/2^+$	3
18882(8)	2322(2)	1.9(2)	1.18(12)	$E2$	$39/2^-$	$35/2^-$	6
18952(6)	4435(4)	0.2(1)				$33/2^+$	3
19093(7)	2242.4(7)	16(1)	1.10(6)	$E2$	$41/2^+$	$37/2^+$	5
19429(7)	2674(1)[b,c]	2.3(6)	0.99(8)	$E2$	$41/2^-$	$37/2^-$	7
19670(6)	1361.9(3)	1.1(5)	0.51(7)	$E2/M1$	$41/2^-$	$39/2^-$	8
	2548(1)	4.0(5)	1.06(8)	$E2$	$41/2^-$	$37/2^-$	8
19834(7)	2006(1)[b]	< 0.1		$(E2/M1)$	$(39/2^+)$	$(37/2^+)$	4
	3804(3)	0.4(1)		$(E2)$	$(39/2^+)$	$35/2^+$	4
19915(5)	3885(3)	0.3(1)	1.05(39)	$(E2)$	$(39/2^+)$	$35/2^+$	4
19929(7)	2323(1)[c]	1.1(3)	1.15(12)	$E2$	$39/2^{(+)}$	$35/2^{(+)}$	10
20523(8)	2495(1)	0.9(2)	1.02(15)	$E2$	$41/2^-$	$37/2^-$	6
20705(7)	1753(2)	< 0.1					3
	2028(1)	< 0.1					3
21094(7)	1424(2)	0.3(1)	0.68(14)	$E2/M1$	$43/2^-$	$41/2^-$	8
	2786(2)	2.0(4)	0.95(13)	$E2$	$43/2^-$	$39/2^-$	8
21256(6)	3295(3)	0.6(2)		$(E2)$	$(43/2^-)$	$39/2^-$	7
21640(8)	2758(2)	1.1(2)	0.94(14)	$E2$	$43/2^-$	$39/2^-$	6
21704(8)	2611(1)	8.0(5)	1.07(6)	$E2$	$45/2^+$	$41/2^+$	5
22048(8)	2214(1)	0.3(1)		$(E2/M1)$	$(41/2^+)$	$(39/2^+)$	4
22578(8)	2649(2)	0.6(2)		$(E2)$	$(43/2^+)$	$39/2^{(+)}$	10
22684(8)	1590(1)	0.6(2)	0.72(11)	$E2/M1$	$45/2^-$	$43/2^-$	8
	3014(2)	0.8(3)	1.07(15)	$E2$	$45/2^-$	$41/2^-$	8
23458(9)	2935(2)	0.4(1)	1.02(37)	$(E2)$	$(45/2^-)$	$41/2^-$	6
23529(9)	4100(4)	0.2(1)		$(E2)$	$(45/2^-)$	$41/2^-$	7
24316(9)	1632(1)	0.4(1)		$(E2/M1)$	$(47/2^-)$	$45/2^-$	8
	3223(3)	0.6(2)		$(E2)$	$(47/2^-)$	$43/2^-$	8
24709(9)	3004(2)	2.5(4)	1.03(7)	$E2$	$49/2^+$	$45/2^+$	5
24768(9)	3128(2)	0.3(1)		$(E2)$	$(47/2^-)$	$43/2^-$	6
25677(10)	3099(3)	0.3(2)		$(E2)$	$(47/2^+)$	$(43/2^+)$	10
26223(10)	3539(3)	0.2(1)		$(E2)$	$(49/2^-)$	$45/2^-$	8
26840(11)	3382(3)	< 0.1		$(E2)$	$(49/2^-)$	$(45/2^-)$	6
28133(11)	3424(1)	0.2(1)	0.93(15)	$E2$	$53/2^+$	$49/2^+$	5
31960(12)	3827(1)	< 0.1		$(E2)$	$(57/2^+)$	$53/2^+$	5
X+1631	1631(1)	0.4(1)			$(J+2)$	(J)	9
X+3647	2016(1)	1.0(2)			$(J+4)$	$(J+2)$	9
X+6005	2358(1)	0.9(2)			$(J+6)$	$(J+4)$	9
X+8812	2807(2)	0.5(1)			$(J+8)$	$(J+6)$	9

[a] Doublet with intense transitions in ^{57}Co or ^{58}Ni.
[b] Gamma-ray energy calculated from level differences.
[c] Doublet structure.
[d] Not shown in the level scheme.

Table 2. DCO-ratios of three different angle combinations and deduced $\delta(E2/M1)$ mixing ratios for a number of $\Delta I = 0$ and stretched $\Delta I = 1$ transitions in ^{59}Cu. For details see text and ref. [17].

E_x (keV)	E_γ (keV)	$R_{30\text{-}53}$	$R_{30\text{-}83}$	$R_{53\text{-}83}$	α_2	δ
			Structures 1 and 2			
914(1)	913.5(2)	0.64(3)	0.44(4)	0.69(3)	0.57	$+0.24(^{11}_{7})$, $\sim +1.7$
1398(1)	484.3(1)	0.78(8)	0.50(8)	0.77(6)	0.58	$+0.05(1)$
1864(1)	465.8(1)	1.03(5)	0.94(7)	1.05(5)	0.59	$-1.19(^{24}_{29})$, $+0.07(^{10}_{11})$
	950.5(2)	0.80(4)	0.65(5)	0.73(4)		$-0.02(5)$, $+4.1(^{11}_{9})$
2389(1)	990.8(2)	0.73(8)	0.48(4)	0.76(5)	0.60	$+0.08(^{10}_{7})$
2663(1)	798.5(2)	0.98(5)	0.90(5)	0.92(4)	0.60	$-0.28(4)$
	1264.4(3)	1.07(8)	1.29(12)	0.80(11)		$-0.48(^{12}_{13})$
3041(1)	1177.5(2)	0.88(7)	0.59(4)	0.71(4)	0.61	$-0.03(1)$
	1643.5(3)	0.78(7)	0.58(3)	0.79(5)		$-0.02(1)$
3328(1)	664.5(2)	0.89(4)	0.76(4)	0.84(4)	0.62	$-0.15(^{5}_{4})$
	741.7(2)	1.03(6)	1.00(9)	1.02(7)		$-0.81(^{22}_{30})$
3445(1)	860.1(2)	0.61(6)	0.25(4)	0.61(5)	0.62	$+0.2 < \delta < +2.6$
4099(1)	653.5(1)	0.99(6)	0.95(5)	0.96(6)	0.63	$-1.04(^{18}_{12}), 0.22(^{12}_{11})$
	770.7(2)	0.92(4)	0.78(4)	0.82(4)		$-0.19(4)$
4902(1)	802.7(2)	0.86(5)	0.82(6)	0.78(7)	0.65	$-0.18(^{6}_{5})$
	1457.3(3)	0.72(6)	0.38(3)	0.59(4)		$+0.21(^{11}_{8})$
5720(1)	818.1(2)	0.88(5)	0.74(4)	0.82(4)	0.66	$-0.15(^{5}_{4})$
6048(2)	1145.5(2)	1.02(7)	0.92(6)	0.84(7)	0.67	$-4.1(^{8}_{16})$, $-0.32(6)$
6609(2)	888.1(2)	0.91(5)	0.75(5)	0.81(5)	0.68	$-0.16(^{5}_{4})$
6795(2)	1370.1(3)	0.77(5)	0.60(4)	0.71(4)	0.69	$0.00(^{6}_{5})$
7051(2)	1331.2(3)	0.83(17)	0.49(11)	0.44(7)		$-0.5 < \delta < 1.7$
7443(2)	833.7(2)	0.94(9)	0.78(5)	0.82(15)	0.69	$-0.20(^{6}_{5})$
8812(2)	1368.7(3)	0.83(7)	0.78(9)	0.80(5)	0.72	$-0.14(6)$
			Structure 3			
6689(2)	1788.1(4)	0.75(9)	0.53(5)	0.70(4)		$+0.05(1)$
7351(2)	1630.7(3)	0.77(6)	0.56(4)	0.72(6)	0.70	$0.02(^{6}_{5})$
	1925.8(7)	1.04(17)	0.48(8)	0.74(8)		$+0.04(^{13}_{11})$
8114(2)	762.9(2)	0.91(9)	0.61(6)	0.82(6)	0.71	$-0.10(^{7}_{6})$
	1505.5(3)	0.73(8)	0.47(6)	0.62(4)		$+0.13(^{10}_{7})$, $+4.4(^{264}_{118})$
8942(2)	827.4(2)	0.91(9)	0.75(5)	0.84(6)	0.73	$-0.18(^{6}_{5})$
	1499.1(10)	0.73(6)	0.63(6)	0.67(6)		$-0.02(^{6}_{5})$
10603(2)	932.1(2)	0.90(7)	0.89(6)	0.76(6)	0.76	$-0.24(5)$
12419(2)	1815.6(4)	0.97(10)	0.88(10)	0.65(6)	0.80	$-0.23(^{8}_{7})$
12808(2)	2204.5(4)	0.92(7)	0.55(4)	0.61(4)	0.81	$0.10(8)$
13527(2)	718.6(1)	1.05(13)	0.68(5)	0.96(7)	0.82	$-0.67(^{21}_{48})$, $+0.58(^{28}_{17})$
	1108.0(2)	0.89(7)	0.63(6)	0.90(8)		$-0.16(^{8}_{11})$
14517(3)	990.8(2)	0.87(10)	0.71(7)	0.82(8)	0.84	$-0.16(6)$
			Structure 4			
7792(2)	2890(1)	0.71(9)	0.62(8)	0.46(7)	0.71	$0.00(^{20}_{8})$
7825(7)	2923(1)	0.94(23)	0.47(14)	0.71(10)	0.71	$-0.05(^{20}_{13})$
8153(2)	327.9(1)	0.94(10)	0.65(11)	0.76(7)	0.71	$-0.13(^{9}_{7})$
	360.9(1)	0.99(7)	0.61(10)	0.67(6)		$-0.15(7)$
	2728(1)	1.03(13)	1.20(13)	0.94(9)		$-0.45(^{10}_{13})$
8727(2)	574.1(1)	0.93(5)	0.71(7)	0.82(5)	0.73	$-0.16(^{12}_{5})$
10276(2)	819.8(2)	1.00(6)	0.73(6)	0.78(6)	0.76	$-0.21(5)$, $-6.3(^{14}_{78})$
12247(2)	1035.0(3)	0.93(8)	0.59(6)	0.64(12)	0.79	$-0.21(^{11}_{10})$
13358(3)	1111.0(6)	0.92(10)	1.12(14)	0.81(9)	0.82	$-0.44(^{12}_{10})$

Table 2. Continued.

E_x (keV)	E_γ (keV)	$R_{30\text{-}53}$	$R_{30\text{-}83}$	$R_{53\text{-}83}$	α_2	δ
			Structure 7			
13194(2)	641.4(1)	1.05(8)	1.06(12)	0.82(6)	0.81	$-2.8(^{5}_{8}), -0.35(7)$
14782(3)	850(1)	1.15(14)	1.24(10)	1.45(24)	0.85	$\delta \approx -1$
15724(3)	942(1)	1.25(13)	0.77(11)	1.12(15)	0.86	$\delta \approx -2$
16755(4)	1031(1)	1.60(14)	1.12(8)	1.13(8)	0.89	$\delta \approx -1$
			Structure 8			
11121(3)	3007(2)	0.79(6)	0.57(6)	0.73(6)	0.77	$-0.03(^{6}_{5})$
	3678(2)	0.47(8)	0.19(5)	0.46(6)		$+0.2 < \delta < +2.0$
11719(3)	598.8(1)	0.76(7)	0.47(4)	0.60(5)	0.78	$+0.06(^{6}_{5})$
12374(3)	654.0(1)	0.78(5)	0.50(4)	0.72(5)	0.80	$+0.01(5), +6.4(^{20}_{18})$
13104(3)	730.0(1)	0.59(6)	0.51(4)	0.75(7)	0.81	$0.74(^{6}_{5})$, $0.05(^{17}_{14})$
14955(4)	1038(1)	0.66(5)	0.35(4)	0.59(5)	0.85	$0.15(^{7}_{5})$
15984(5)	1028(1)	0.55(5)	0.43(5)	0.82(9)	0.87	$0.15(^{7}_{5})$
17123(5)	1139(1)	1.05(13)	0.55(6)	0.53(5)	0.89	$-0.69(^{8}_{6})$
18308(6)	1184.7(10)	0.72(8)	0.70(6)	0.61(11)	0.92	$-0.12(5)$
19670(6)	1361.9(3)	1.07(24)	0.51(7)	0.54(9)	0.94	$-0.02(1)$
21094(7)	1424(2)	1.29(38)	0.68(14)	1.00(24)	0.97	$-0.27 < \delta < -0.02$

transitions. The results are comprised in table 2 together with the respective $R_{\rm DCO}$(30-53) and $R_{\rm DCO}$(53-83) ratios. The phase convention of Rose and Brink [19] is used for the mixing ratios. The alignment coefficients α_2 were fixed using the relation $\alpha_2 = 0.55 + 0.02 \cdot E_x({\rm MeV})$ and uncertainties $\Delta\alpha_2 \pm 0.05$. For more details we refer to ref. [17]. As an example, fig. 2 provides the analysis of the 771 keV $13/2^- \rightarrow 11/2^-$ transition. The weighted mean of the three consistent solutions for the mixing ratio, $\delta(E2/M1) = -0.19(4)$, is given in table 2. Despite being unphysical, neither very large positive nor very large negative solutions for the mixing ratios are consistent for all three angle combinations.

The lifetimes of the states at the top of the rotational bands in the mass $A \approx 60$ region are in the femtosecond regime. Therefore, they likely decay while the ^{59}Cu nuclei are slowing down in the thin target foil. The Doppler correction of the γ-ray lines is performed using the velocity of the recoils *after* the target, such that the peaks of transitions below some 13 MeV excitation energy (cf. fig. 1) are lined up in γ-ray spectra taken at different Ge-detector angles Θ. Thus, the γ-rays emitted during the slowing-down process in the target have additional Doppler shifts, particularly in spectra of Ge-detectors at forward and backward angles. This effect represents an important experimental tool to determine (average) transitional quadrupole moments of highly excited states [20]. From the additional Doppler-shifts experimental $F(\tau)$-values can be derived for a γ-ray transition according to

$$F(\tau) = \langle v(t)\rangle / \langle v_0\rangle \,, \qquad (2)$$

where $\langle v(t)\rangle$ denotes the average velocity of recoils at the time of the emission of the γ-ray and $\langle v_0\rangle$ is the average initial recoil velocity of the residual nuclei.

The heavy-ion fusion-evaporation reaction $^{28}{\rm Si} + {}^{40}{\rm Ca}$ takes place at a given point in the thin ^{40}Ca target. The position of the exact point is not measurable. After the beam slowed down in a fraction of the target, the compound nucleus is formed, which then starts to evaporate light charged particles, in the present case two α-particles and one proton. The particle evaporation (mainly α-particles) determines both the direction and the magnitude of the initial ^{59}Cu velocity vector $\mathbf{v}_0$. Based on the measured energies and directions of the evaporated particles it is possible to reconstruct event by event the direction of $\mathbf{v}_0$ of the ^{59}Cu recoils. Assuming a random interaction point in the target and accounting for the corresponding energy loss of the beam in the front part of the target foil, the value of $\mathbf{v}_0$ can be reliably estimated, also on an event-by-event basis.

The average initial recoil velocity $\langle v_0\rangle$ is, of course, independent of the excitation energy of the residual nucleus. However, it turns out that there is an experimental bias, which does induce such a dependency. The effect is illustrated in fig. 3, which provides the *observed* average initial velocities $\langle v_0\rangle$ of ^{59}Cu recoils as a function of the excitation energy E_x. Only events which passed the usual criteria used in the analysis of ^{59}Cu, *i.e.*, two α-particles and one proton detected in Microball and proper TE selection, were used to generate fig. 3. These events were sorted into a matrix E_γ *vs.* v_0, and distributions of the latter were produced by gating on a number of γ-ray transitions. The excitation energy on the x-axis of fig. 3 is defined by the depopulating γ-ray, while the y-axis is the mean value of

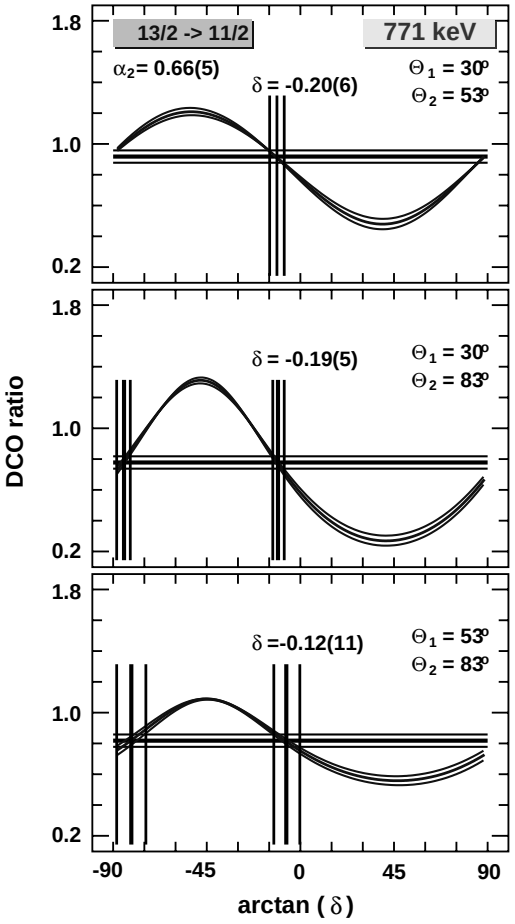

Fig. 2. Analysis of DCO-ratios of the 771 keV $13/2^- \rightarrow 11/2^-$ transition using three different detector angle combinations. The experimental DCO-ratios are represented by the horizontal lines. The DCO-ratios calculated as a function of the multipole mixing ratio $\delta(E2/M1)$ for the given alignment (including uncertainties) are shown by the three curves in each panel. The crossings of the curves with the experimental DCO-ratio mark possible solutions for the mixing ratio, indicated by the vertical lines.

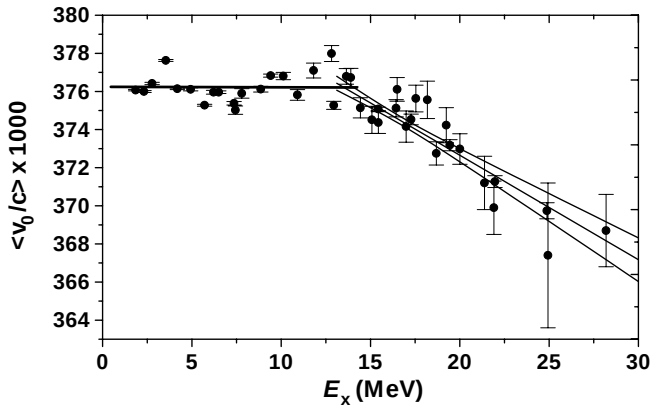

Fig. 3. The average *observed* initial velocity of ^{59}Cu recoils as a function of the excitation energy.

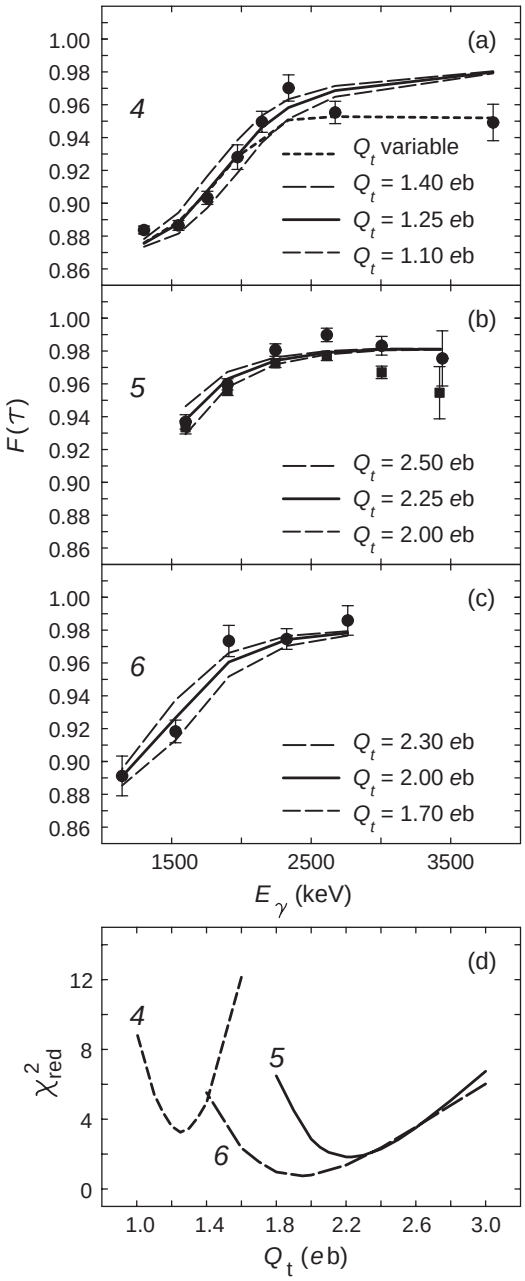

Fig. 4. Uncorrected (squares), corrected (circles), and simulated (solid and dashed lines) $F(\tau)$-values *versus* γ-ray energy for the rotational structures 4 (panel (a)), 5 (panel (b)), and 6 (panel (c)). Panel (d) shows the reduced χ^2 as a function of the presumed average quadrupole moment for these three bands. See text for details.

the corresponding v_0 distribution. Up to $E_x \sim 13$ MeV the observed average velocity is, as expected, constant at $\langle v_0 \rangle = 0.03762(5)c$. However, beyond $E_x = 13$ MeV $\langle v_0 \rangle$ is decreasing, and a simple linear parametrisation yields $\langle v_0(E_x) \rangle / c = 0.03831(7) - 5.31(39) \cdot 10^{-5} E_x$ (MeV). The population of a residual nucleus at higher and higher excitation energy implies that there is on average less and less phase space available for the evaporated charged particles. Therefore, their average energies have to decrease with increasing excitation energy of the final residue.

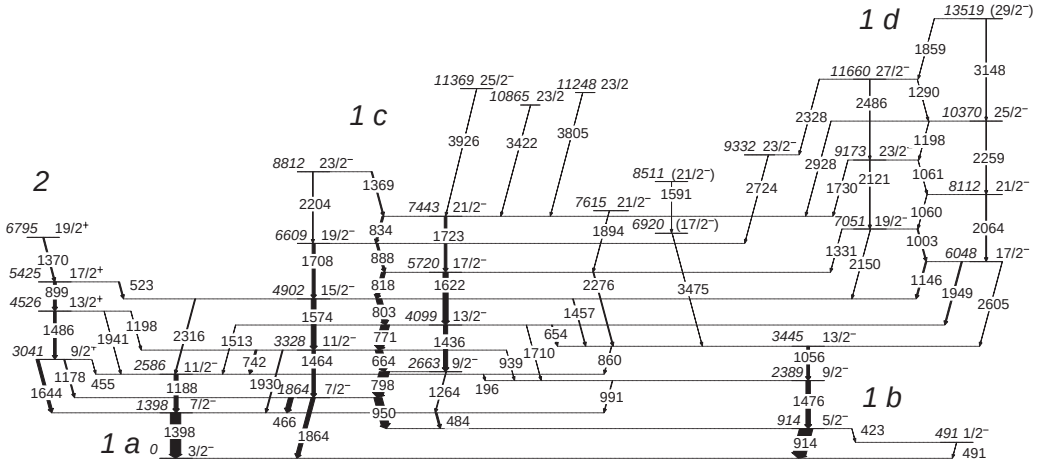

Fig. 5. Structures 1 and 2 of the level scheme of ^{59}Cu. Energy labels are in keV. The widths of the arrows are proportional to the relative intensities of the γ-rays. Tentative levels and transitions are dashed.

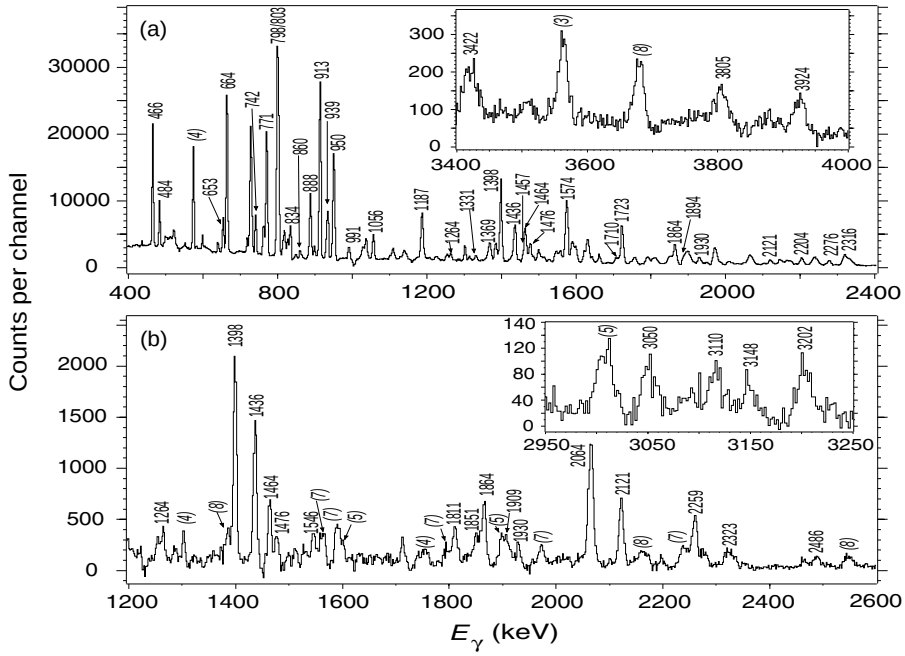

Fig. 6. Gamma-ray spectra in coincidence with the 818 keV $17/2^- \rightarrow 15/2^-$ (panel (a)) and 1949 keV $17/2^- \rightarrow 13/2^-$ (panel (b)) transitions. Transitions known to belong to ^{59}Cu [24] and the new transitions from structures 1, 2, and 10 are labelled with their energies in keV. Numbers in parentheses on top of some peaks indicate the structure within the ^{59}Cu level scheme to which they belong.

A reduced average particle energy causes a less probable *observation*, in particular of α-particles in the backward-angle hemisphere of Microball, because it is increasingly difficult for the particles to penetrate the absorbers in front of the Microball detector elements. However, for the present analysis of ^{59}Cu we always demand two detected α-particles, which thus have to be detected at more and more forward angles the higher the excitation energy of ^{59}Cu is. This leads to an apparent lower average initial velocity of the ^{59}Cu recoils as seen in fig. 3. Consequently, for the present case eq. (2) has to be replaced with

$$F(\tau) = \langle v(t) \rangle / \langle v_0(E_x) \rangle, \qquad (3)$$

using the parametrisation of $v_0(E_x)$ mentioned above.

The consequence of the $v_0(E_x)$ dependence on the $F(\tau)$ analysis is indicated in fig. 4(b). The squares represent the uncorrected experimental $F(\tau)$-values of the yrast superdeformed band 5 using eq. (2). A drastic drop is observed for the last two data points, which is less pronounced for the circles, which correspond to the corrected $F(\tau)$-values according to eq. (3). The variation of the average initial velocities of the ^{59}Cu recoils hence manifests itself as an overestimated decrease of the $F(\tau)$-values at higher excitation energies, which (wrongly) suggests a smaller transitional quadrupole moment Q_t for the higher-lying states. In fact, $Q_t \sim 0.5\ eb$ would be necessary

to explain the uncorrected data point of the 3424 keV line. This is completely at variance both with the previously measured average quadrupole moment of band 5, $\overline{Q}_{\rm t} = 2.24(20)$ eb, which has also been confirmed in the present work, and the fact that this superdeformed band is expected to terminate at a much higher spin of $I = 65/2$ [5]. The circles in panels (a) and (c) in fig. 4 show the corrected experimental $F(\tau)$-values of band 4 and 6, respectively. For the other bands the average quadrupole moments could not be deduced due to either low intensity or unavoidable impurities in the respective γ-ray spectra.

The γ-decay of bands 4, 5, and 6 was modeled with the LINESHAPE code [23]. Thereby, the slowing-down process in the target was simulated with the shell-corrected Northcliffe and Schilling stopping powers [22], and using 10000 initial velocity vectors $\mathbf{v}_0$, which were randomly selected from events associated with ^{59}Cu residual nuclei. The result of the Monte Carlo procedure is stored in 10000 time-dependent velocity histograms, *i.e.*, $\mathbf{v}_i(t)$, $i = 1, ..., 10000$, in time intervals of $\Delta t = 0.2$ fs up to $t_{\rm max} = 0.8$ ps. In a second step, these velocity histograms were converted into time-dependent velocity profiles as seen by the Ge-detectors at 35°, 50°, 90°, 130°, and 145°, the γ-ray spectra of which were used to obtain the experimental $F(\tau)$-values as described above. Finally, all curves but one in fig. 4 represent simulations of the $F(\tau)$-values assuming constant in-band quadrupole moments and three-step side-feeding cascades having the same quadrupole moment as the in-band transitions. The solid lines in fig. 4(a), (b), and (c) represent the best least-square fits to the data points, while the dashed lines mark the quadrupole moments for which $\chi^2_{\rm red} = \chi^2_{\rm red,min}+1$. The χ^2-dependences on the quadrupole moments are depicted in fig. 4(d) for the three bands. The numerical results are to be discussed in the following section, including the dotted curve in fig. 4(a). Systematic uncertainties due to the simulation of the slowing-down process are not included in the numerical results. They are typically on the order of 10%.

3 Results

Previously, excited states in ^{59}Cu had been studied up to spin and parity $I^\pi = 17/2^-$ at an excitation energy $E_x = 5721$ keV using the light-ion–induced reaction ^{58}Ni(^{3}He, pn) at bombarding energies $E_{\rm lab} = 15$–27 MeV [24]. Early results of our study of ^{59}Cu focused on the yrast superdeformed band [5] and prompt proton emission of bands 5 and 6 [7].

Due to the complexity of the level scheme of ^{59}Cu, each structure or rotational band labelled in fig. 1 is going to be presented separately. The corresponding parts of the level scheme will be shown in greater detail, and they are accompanied by $2\alpha 1p$- and TE-gated γ-ray spectra measured in coincidence with selected and representative transitions. The spectra will illustrate either the in-band or the linking transitions to the near-spherical states (structures 1 and 2), or to some other excited rotational band. Previous spin and parity assignments of the states were confirmed [5,24]. With the exception of structure 9, all excited rotational bands are connected to the low-spin states by a number of linking transitions. This allowed firm spin and parity assignments to the lowest states in the bands, because the transitions at the bottom of the bands are either sufficiently intense or clean to distinguish between stretched quadrupole or dipole character of some of the more intense linking transitions. The tentative spin and parity assignments to the states near the top of the bands are based on their regular rotational behaviour.

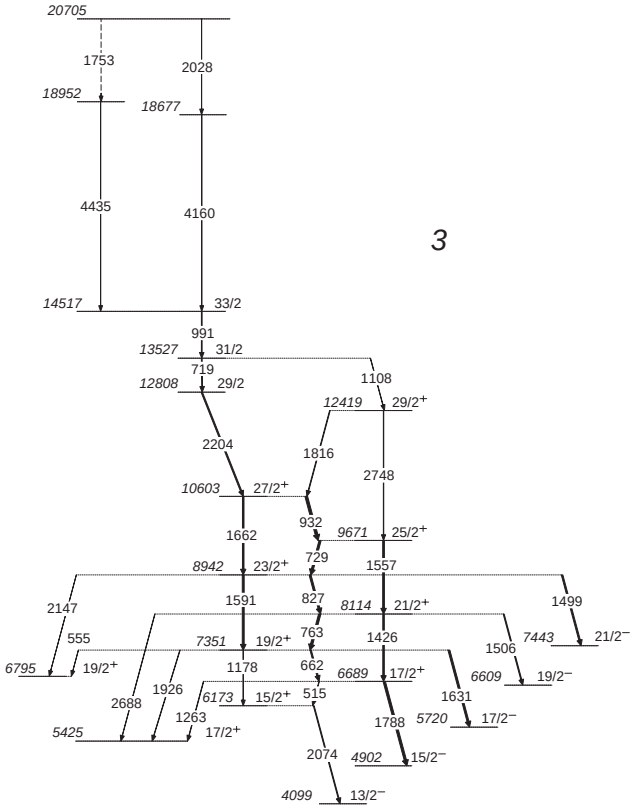

Fig. 7. Structure 3 of the level scheme of ^{59}Cu. See caption of fig. 5 for details.

3.1 Structures 1 and 2

Figure 5 provides the low-spin part of the present decay scheme, which includes the structures labelled 1 and 2 in fig. 1. It is consistent with the previously reported high-spin scheme in ref. [24], but extending it noticeably. In particular, the assignment of positive parity to states belonging to structure 2 is supported by the mixing ratios of the 1178 and 1644 keV lines, which depopulate the 3041 keV $9/2^+$ level. Both are close to zero (see table 2), which is in line with their parity-changing $E1$ character. Additional weak transitions connecting structures 2 and 1 could be added, as well as the 1370 keV line on top of structure 2.

Structure 1 has been split into four parts: While structure 1d is new, sequences 1a, 1b, and 1c represent the excited states built upon the $(p_{3/2})$ $3/2^-$ ground state,

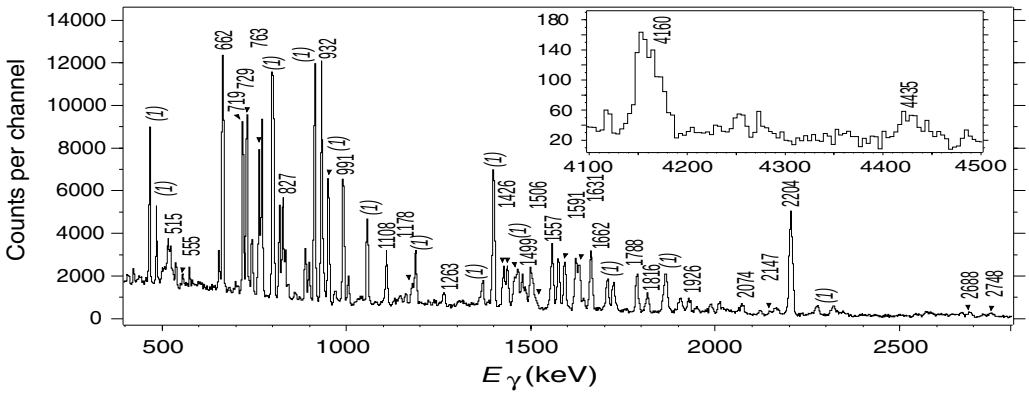

Fig. 8. Sum of the γ-ray spectra in coincidence with the 719 and 991 keV transitions in band 3. See text and caption of fig. 6 for details.

the $(f_{5/2})$ $5/2^-$ level at 914 keV, and the $(f_{7/2}^{-1})$ $7/2^-$ state at 1864 keV [24]. The latter has been extended up to spin $23/2^-$, and several new interband transitions have been observed. A γ-ray spectrum in coincidence with the 818 keV transition, which depopulates the 5720 keV $17/2^-$ level in structure 1c, is shown in fig. 6(a). The sequence of the $\Delta I = 1$ transitions at 664, 771, 798, 803, 834, 888, and 1369 keV is clearly visible, along with the accompanying stretched quadrupole transitions. Some other pronounced peaks in fig. 6(a), which were found to belong to ^{59}Cu as well, are labelled only with their structure identification number. Examples of new, weak interband transitions are those at 939, 1457, 1710, or 2316 keV. To take one example, the 1710 keV $13/2^- \rightarrow 9/2^-$ line is a doublet with the 1708 keV $19/2^- \rightarrow 15/2^-$ transition, but the former has to be absent in fig. 6(a), because both the 818 and 1708 keV lines populate the 4902 keV $15/2^-$ level, and consequently they are not in coincidence with each other. The 1710 keV line matches also the energy difference between the levels at 4099 and 2389 keV, while the $\gamma\gamma\gamma$-cube analysis ultimately justifies its placement in the level scheme. Doublets with intense transitions from ^{58}Ni [25] are present at 939 and 1457 keV in fig. 6(a). In addition, there are transitions at 932 keV (structure 3), 935 keV (structure 4), and 942 keV (structure 7), which contribute to the 939 keV peak in fig. 6(a). The 939 keV line matches the energy difference between the levels at 3328 and 2389 keV, while the 1457 keV line matches the difference in energy between the levels at 4902 and 3445 keV. Again, the cube analysis allows for a definite placement. It is also worth mentioning that the previously mentioned sequence of $\Delta I = 1$ transitions in structure 1c have nearly constant mixing ratios of $\delta \sim -0.20$, while the quadrupole admixture of interband transitions vary between $\delta \sim -1.2$ and $+4.0$.

The right-hand side of fig. 5 shows the new structure 1d ranging from the 6048 keV $17/2^-$ state to the 13519 keV $(29/2^-)$ state. Similar to structure 1c, into which it mainly decays, it comprises almost equally intense dipole and parallel quadrupole transitions. Figure 6(b) provides the γ-ray spectrum in coincidence with the 1949 keV transition, which depopulates the 6048 keV level at the bottom of the structure. It clearly reveals the transitions belonging to structure 1d itself and the low-lying transitions in structures 1a, 1b, and 1c, respectively. In addition, lines arising from band 10 are visible at, *e.g.*, 1811, 1851, 1909, 2276, 2323, 3050, and 3110 keV. Band 10 feeds the structure 1d at high spin.

Finally, there are several states which do not seem to belong to any apparent band-like structure, namely at 6920, 7615, 8511, 9332 and three levels at ~ 11 MeV. Most of the corresponding γ-ray lines can be seen in the inset of fig. 6(a), *e.g.*, at 3422, 3805, and 3926 keV. It is interesting to note that it is possible to determine DCO-ratios even for such weak transitions: The $R_{\rm DCO}$(30-83) value of the 3805 keV transition is 0.62(16), which suggests dipole character, and thus a spin assignment of $I = 23/2$ to the level at 11248 keV, while the parity of the level remains undetermined.

3.2 Structure 3

Figure 7 focuses on band 3. The lower part of the band up to spin $I^\pi = 27/2^+$ at an excitation energy $E_x = 10.60$ MeV has already been shown in ref. [5]. The γ-ray spectrum in fig. 8 is the sum of the spectra in coincidence with the 719 keV $31/2^+ \rightarrow 29/2^+$ and 991 keV $33/2^+ \rightarrow 31/2^+$ transitions. New transitions at, for example, 1263, 1816, 2147, or 2204 keV are clearly seen. The inset shows the high-energy portion of this spectrum including the weak 4160 and 4435 keV transitions, for which no DCO-ratios could be determined. The core of structure 3 is the strongly coupled band of $\Delta I = 1$ and parallel $E2$ transitions between the $15/2^+$ level at 6173 keV and the $29/2^+$ level at 12419 keV. The decay of band 3 proceeds both into negative-parity states of structure 1c and positive-parity states of structure 2. Towards the top structure 3 turns into a rather irregular sequence of levels, which fades out at an excitation energy of $E_x = 20.71$ MeV.

The assignment of positive parity to band 3 is based on its intermediate position between structures 2 and the yrast superdeformed band 5 (see also below and ref. [5]). For example, the 12039 keV state in band 5 decays to the 8114 keV state in band 3 by the 3922 keV stretched

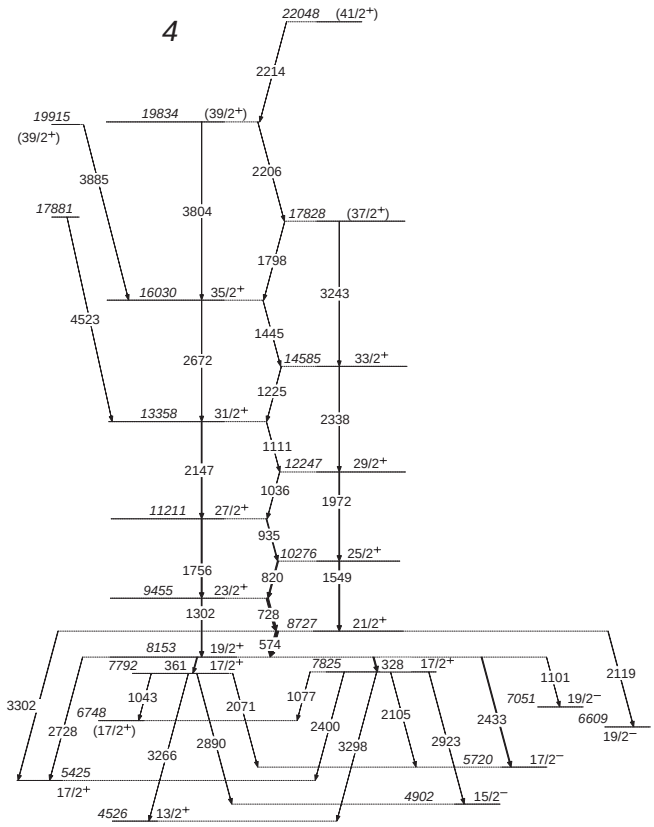

Fig. 9. Structure 4 of the level scheme of ^{59}Cu. See caption of fig. 5 for details.

quadrupole transition. In turn, the 8114 keV state is connected to the yrast $17/2^+$ state at 5425 keV via the 2688 keV line, fixing the spin and parity of the level at 8114 keV to $21/2^+$. Positive-parity assignment to band 3 is further supported by the mixing ratios of the 1499, 1506, and 1788 keV $E1$ transitions, which are all close to zero. Finally, it is worth noting that the mixing ratios of the in-band $\Delta I = 1$ transitions at 763, 827, 932, and 1816 keV lie around $\delta \sim -0.20$, similar to what has been observed for structure 1c.

3.3 Structure 4

Structure 4, which is depicted in fig. 9, has previously been published up to a spin and parity of $I^\pi = 35/2^+$ at an excitation energy of $E_x \sim 16$ MeV [5]. With the present data set it could be extended up to $I^\pi = (41/2^+)$ at $E_x = 22.20$ MeV. Figure 10 shows the sum of γ-ray spectra in coincidence with transitions at 328, 361, and 574 keV, which are placed at the bottom of the sequence. Similar to structure 3, band 4 consists of a strongly coupled rotational sequence. The decays from the low-lying $17/2^+$, $19/2^+$, and $21/2^+$ states connect band 4 mainly to structures 2 and 1c. From all structures discussed so far, band 4 follows the rotational $E \sim I(I+1)$ rule closest. This scheme is only broken at the highest spins with the transitions at 3243 and 3804 keV, respectively. These transitions are highlighted in the inset of fig. 10 together with the 3885, which "side-feeds" band 4, and the $E_\gamma \sim 3$ MeV linking transitions.

Table 3. In-band quadrupole moments Q_t and side-feeding quadrupole moments Q_s for the spin-dependent $F(\tau)$ simulation of band 4 represented by the dotted curve in fig. 4(a). See text for details.

E_x (keV)	19834	17828	16030	14585	13358 to 9455
Q_t (eb)	0.8	1.0	1.1	1.3	1.3
Q_s (eb)	0.3	0.6	0.8	1.0	1.3

The regular behaviour of band 4 along with the DCO-ratio analysis provide the basis for the spin and parity assignments of the states up to the 22048 keV $(41/2^+)$ level. Positive parity has been assigned to band 4 previously [5]. Additional arguments, which are similar to those invoked for the parity assignment of band 3, can be applied for the case of band 4. For example, the mixing ratio $\delta = -0.45(^{19}_{13})$ deduced for the 2728 keV $19/2^+ \rightarrow 17/2^+$ transition suggests a mixed $E2/M1$ transition, while the mixing ratios determined for some of the (high-energy) parity-changing $E1$ transitions are consistent with zero (cf. table 2). Once again, the in-band $\Delta I = 1$ transitions have nearly constant mixing ratios on the order of $\delta = -0.20$.

It has been possible to deduce an average quadrupole moment of band 4 in the spin range 19/2–33/2. Figure 4(a) shows the experimental data points of $F(\tau)$-values together with four simulations. The experimental points correspond to the mean values of the stretched quadrupole and $\Delta I = 1$ transitions depopulating the same level, if applicable. The analysis assuming a constant quadrupole moment in the band (see sect. 2) yields $\overline{Q}_\mathrm{t} = 1.25(^{13}_{10})$ eb. At high spin, however, a band termination effect is clearly visible —the $F(\tau)$-value of the 3804 keV $(39/2^+) \rightarrow 35/2^+$ transition is well below the simulations assuming constant quadrupole moments, which suggests a decreasing quadrupole moment with increasing spin. In fact, using the spin-dependent in-band quadrupole moments Q_t and side-feeding quadrupole moments Q_s listed in table 3, the simulated dotted curve in fig. 4(a) is obtained. Its $\chi^2_\mathrm{red} = 2.6$ is lower than the χ^2_red minimum of band 4 in fig. 4(d).

Finally, both the 7792 and 7825 keV $17/2^+$ states revealed a weak proton decay branch into the 4^+ yrast level of ^{58}Ni [9].

3.4 Structure 5

Figure 11 shows the low-spin part of structure 5 and its comprehensive discrete-energy decay-out scheme. On top of the 16851 keV $37/2^+$ level the band comprises five additional stretched quadrupole transitions with 2242, 2611, 3004, 3424, and 3827 keV [5], leading to the state with the largest spin ($I = (57/2)$) and excitation energy ($E_x = 32.0$ MeV) in the level scheme of ^{59}Cu (see fig. 1). Although searched for, a continuation of this superdeformed band at high spins could not be established

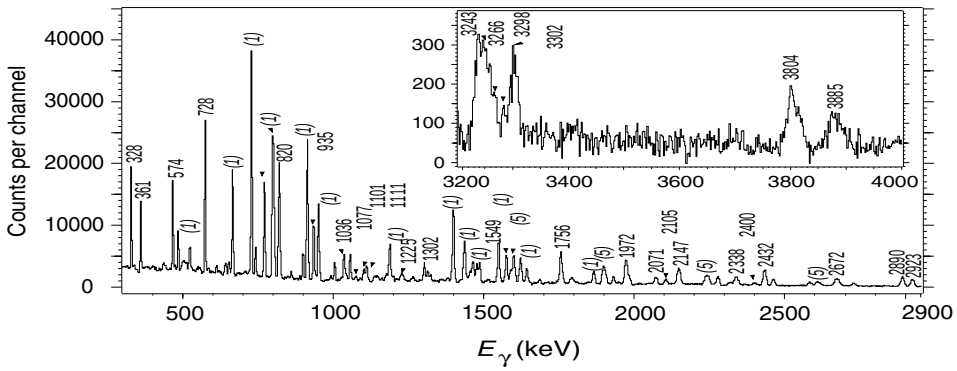

Fig. 10. Sum of γ-ray spectra in coincidence with the 328, 361, and 574 keV transitions in band 4. See text and caption of fig. 6 for details.

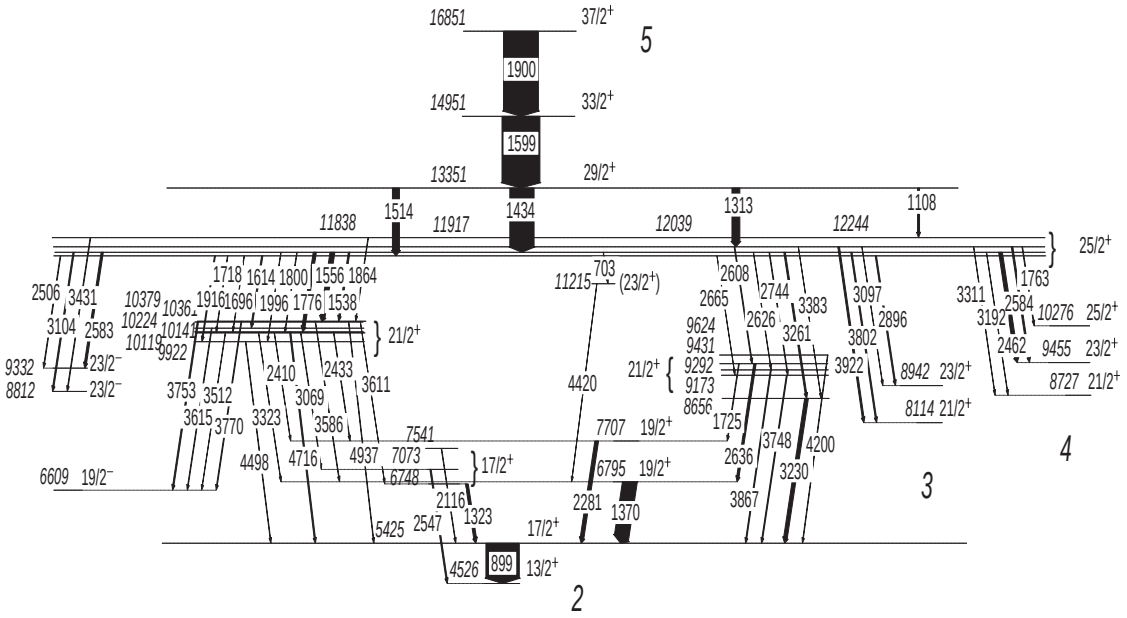

Fig. 11. Structure 5 of the level scheme of ^{59}Cu. See caption of fig. 5 for details.

from the present data set. The complex connection of the superdeformed band to the low-spin states of structures 1, 2, 3, and 4 via high-energy single- or double-step weak linking transitions certainly represents the most complete decay-out scheme from a superdeformed structure to date. It does also contain two weak proton decay branches, namely from the $25/2^+$ states at 11917 and 12039 keV, respectively [7,9]. The decay-out scheme is discussed in detail in ref. [26].

The comprehensive decay-out scheme could be derived from dedicated and subtle triple-γ-coincidence relationships. Figure 12 provides three examples. Figure 12(a) shows a γ-ray spectrum in coincidence with the transition at 4937 keV and any of the 899, 1599, 1644, 2242, or 2611 keV transitions in structure 2 or band 5, respectively. Despite the very weak relative intensity of the 4937 keV line ($I_{\rm rel} = 0.3(2)$ %), the 1556 keV $25/2^+ \rightarrow 21/2^+$ transition, the band members up to the 3004 keV line, as well as the 1178, 1188, 1398, 1486, and 1644 keV transitions in the first minimum (cf. fig. 5) are clearly (and exclusively) visible in this double-γ–gated spectrum. A second example of the discrimination of weak decay-out lines is presented in fig. 12(b) and (c). While both spectra are in coincidence with a peak at $E_\gamma \sim 3750$ keV, panel (b) is additionally in coincidence with the 899 or 1644 keV transitions in structure 2 and panel (c) is additionally in coincidence with the 1599, 2242, or 2611 keV lines in band 5. Clearly, both spectra show a peak at 2744 keV, which gives rise to the 2744–3748 keV sequence between the 11917 and 5425 keV levels. However, the presence of the 1556 keV line as well as weak peaks at, *e.g.*, 1574, 1622, and 1708 keV in fig. 12(c) provide evidence for the parity-changing 3753 keV transition connecting the 10361 keV $21/2^+$ and 6609 keV $19/2^-$ levels.

The quadrupole character of the in-band transitions [5] is confirmed by the present $R_{\rm DCO}$(30-83) ratios in table 1. The four transitions at 1108, 1313, 1434, and 1514 keV, which depopulate the 13351 keV $29/2^+$ level, have also $R_{\rm DCO}$(30-83) values consistent with stretched quadrupole character. This leads to a spin and parity assignment of

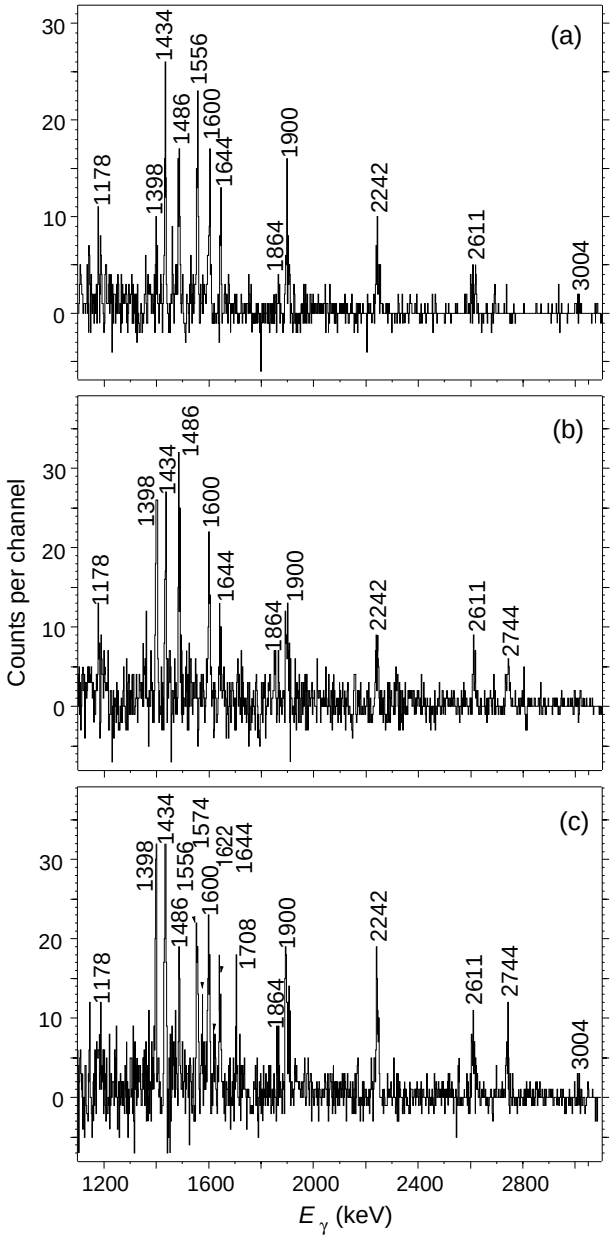

Fig. 12. Gamma-ray spectra with respect to the decay-out regime of the superdeformed band 5. The spectrum in panel (a) is measured in coincidence with the 4937 keV transition and one of the 899, 1599, 1644, 2242, or 2611 keV transitions. Panels (b) and (c) are in coincidence with $E_\gamma \sim 3750$ keV and either the 899 or 1644 keV lines (b) or the 1599, 2242, or 2611 keV lines (c). See text and caption of fig. 6 for details.

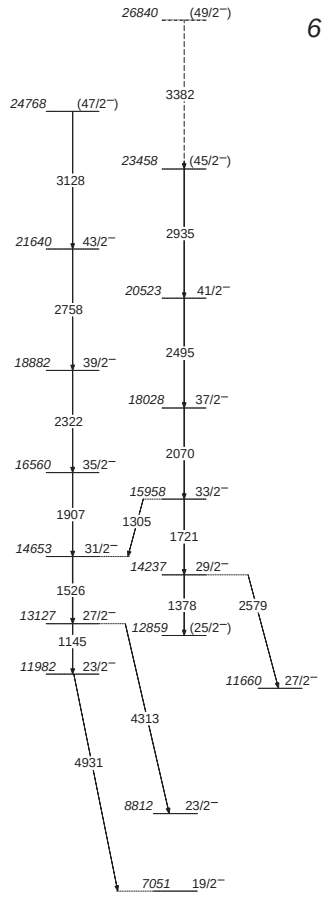

Fig. 13. Structure 6 of the level scheme of ^{59}Cu. See caption of fig. 5 for details.

$25/2^+$ to the corresponding four levels at $E_x \sim 12.0$ MeV. DCO-ratios could also be determined for some of the linking transitions. For example, the 3230 keV transition has $R_{\rm DCO}(30\text{-}83) = 1.07(12)$, which leads to a $21/2^+$ assignment of the 8656 keV level. This assignment allowed us to assign quadrupole character to the 3261 keV transition, which has a consistent $R_{\rm DCO}(30\text{-}83) = 0.87(15)$. In turn, the value $R_{\rm DCO}(30\text{-}83) = 0.48(19)$ of the 2896 keV provides an example for a (mixed) $\Delta I = 1$ transition. The spin and parity of most of the intermediate $21/2^+$ states can be fixed, because they are eventually connected to the 5425 keV $17/2^+$ level and one of the four $25/2^+$ states mentioned above with a single γ-ray transition. An exception is the spin of the level at 11215 keV, which tentatively is assigned to $23/2^+$ based on yrast arguments.

The result of the $F(\tau)$ analysis for band 5, which is shown in panels (b) and (d) of fig. 4, is an average quadrupole moment of $\overline{Q}_{\rm t} = 2.23(^{27}_{22})$ eb. This is in perfect agreement with the previously reported number [5]. Despite the fact that the individual experimental $F(\tau)$-values have rather small uncertainties, the corresponding $\chi^2_{\rm red}$ distribution in fig. 4(d) is relatively shallow, which is mainly due to the lack of data points at lower γ-ray energies: Either lack of statistics or doublets close to the four $29/2^+ \rightarrow 25/2^+$ transitions prevent the extraction of reliable data points to them. Furthermore, the data points of the 2242 and 2611 keV transitions lie significantly above the simulated curves, which may be taken as a sign of spin-dependent deformations in band 5. For example, a simulation with a constant $Q_{\rm t} = 2.40$ eb between the 13351 and 21794 keV levels, which thereafter drops by 0.15 eb for each state, provides a $\chi^2_{\rm red}$ which is as low as the best fit using the constant $\overline{Q}_{\rm t} = 2.23$ eb.

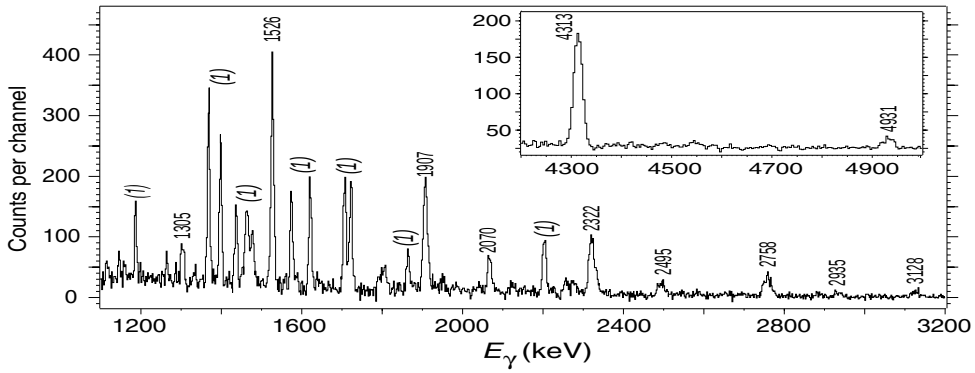

Fig. 14. Gamma-ray spectrum generated by gating on the transition at 4313 keV placed in structure 6. The inset shows the high-energy portion of the spectrum measured in coincidence with the 1526 keV transition. See text and caption of fig. 6 for details.

3.5 Structure 6

Structure 6 is illustrated in fig. 13. It consists of two parallel rotational bands. The band on the left-hand side has been published previously up to spin $I^\pi = 43/2^-$, and a proton decay branch from the level at 11982 keV has been identified [7]. From the present experiment, a 3128 keV line could be added on top of the band, extending it to an excitation energy of $E_x = 24.8$ MeV.

The band on the right-hand side of fig. 13 is connected to the known band through a transition at 1305 keV, which depopulates the 15958 keV level. There is also a transition at 2579 keV linking structure 6 with structure 1d. The main spectrum in fig. 14 is measured in coincidence with the high-energy 4313 keV linking transition, which has a relative intensity of $I_{\rm rel} = 1.4(2)\%$. One can clearly notice the connection between the two bands at 1305 keV, the in-band transitions at 1526, 1907, 2322, 2758, and 3128 keV of the left structure, and the transitions at 2070, 2495, 2935 keV of the right structure. The last, tentative transition at 3382 keV is observed in the $\gamma\gamma\gamma$-cube in coincidence with the in-band transitions. The inset in fig. 14 provides the high-energy portion of the γ-ray spectrum in coincidence with the 1526 keV transition. It focuses on the linking transitions at 4313 and 4931 keV, which connect structure 6 into the low-spin states.

The previous spin and parity assignment to band 6 [7] is confirmed by the DCO-ratio of the 4313 keV linking transition, $R_{\rm DCO}$(30-83) = 0.97(11), which indicates its stretched quadrupole character. The quadrupole character of most of the in-band transitions is based on their $R_{\rm DCO}$(30-83) ratios (see table 1), for example, $R_{\rm DCO}$(30-83) = 1.19(13) and 1.02(15) for the 2070 and 2495 keV lines, respectively. However, the DCO-ratio of the 1305 keV transition is $R_{\rm DCO}$(30-83) = 0.48(8), which fixes the spin of the 15958 keV level to $I^\pi = 33/2^-$. The parallel 1721 keV in-band transition has a stretched $E2$ character, which means that the 14237 keV state has spin $I = 29/2$. The $R_{\rm DCO}$(30-83) = 0.85(14) for the 2579 keV transition, which depopulates the 14237 keV level, is consistent with mixed $E2/M1$ character, thus providing the negative parity. Based on the rotational behaviour of structure 6, tentative spin assignments are suggested to the topmost states as well as to the 12859 keV level at the bottom.

The $F(\tau)$ analysis for the band on the left-hand side of structure 6, which is illustrated in panels (c) and (d) of fig. 4, yields an average quadrupole moment of $\overline{Q}_{\rm t} = 1.95(^{33}_{25})$ eb. The number is only slightly lower than the result for the yrast superdeformed band 5. The quoted errors include only statistical uncertainties.

3.6 Structure 7

Figure 15 shows structure 7. It consists of two rotational bands, which at low-spin are connected by several $\Delta I = 1$ transitions. The topmost state of structure 7 is located at an excitation energy $E_x = 23.5$ MeV and has spin and parity $I^\pi = (45/2^-)$. Structure 7 is linked into states of structures 1, 3, and 4 by a number of transitions. The 1560 and 1806 keV transitions on the right-hand side of fig. 15 provide a connection to band 8.

The transitions which depopulate the 12552 and 11936 keV levels are highlighted in the coincidence spectrum of fig. 16(a), and fig. 16(b) shows a γ-ray spectrum in coincidence with the 4100 keV $(45/2^-) \rightarrow 41/2^-$ transition. This transition on top of structure 7 has a relative intensity as little as $I_{\rm rel} = 0.2(1)$. Nevertheless, the spectrum reveals unequivocal peaks at the energies of the lower-lying transitions in structure 7, *e.g.*, at 1589, 1972, or 2674 keV, and even some transitions in the decay-out regime are visible at, for example, 1476 or 2591 keV.

The spin and parity assignment of band 7 is based on the multiple paths which connect it with the low-spin states and structure 8. For example, the DCO-ratios of the 2277 and 2591 keV lines are in line with stretched dipole character and mixing ratios close to $\delta \sim 0$, while the 1560 and 2824 keV transitions have DCO-ratios consistent with stretched quadrupole character. This implies consistently that the former transitions are parity-changing electric dipole transitions. The sequence of the 1083 and 3299 keV transitions provide independent evidence for the $29/2^-$ assignment to the 13194 keV state. The quadrupole character of the in-band transitions is consistent with their $R_{\rm DCO}$(30-83) ratios, and several $\delta(E2/M1)$ mixing ratios

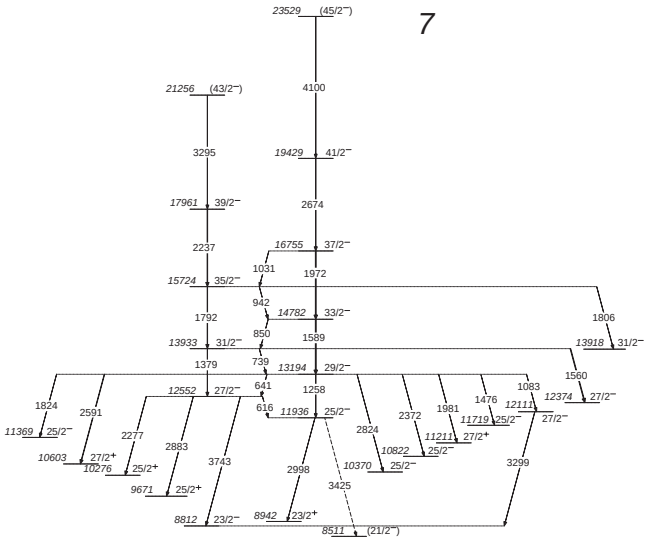

Fig. 15. Structure 7 of the level scheme of ^{59}Cu. See caption of fig. 5 for details.

could be determined for the $\Delta I = 1$ inter-band transitions. At high spin, the tentative assignments are based on the regular rotational behaviour of band 7. Limited statistics and/or doublet structures prevented a reliable $F(\tau)$ analysis in this case.

3.7 Structure 8

Structure 8 is displayed in fig. 17. Similar to band 7 it consists of two parallel bands which reach spins and parities of $I^\pi = 47/2^-$ at an excitation energy $E_x = 24.3$ MeV, and $I^\pi = 49/2^-$ at an excitation energy $E_x = 26.2$ MeV, respectively. At low spins band 8 is almost exclusively connected to structure 1 including high-energy γ-rays up to 5 MeV. Some of them are depicted in the inset of fig. 18, which represents the high-energy portion between 4 and 5 MeV of summed γ-ray spectra in coincidence with the 1042 and 1385 keV transitions situated at the bottom of band 8. The main part of fig. 18 represents a spectrum in coincidence with the inter-band 599 keV $25/2^- \rightarrow 23/2^-$ transition. Both the in-band stretched quadrupole and inter-band $\Delta I = 1$ transitions are clearly visible along with the low-spin yrast cascade of structure 1.

Based on the DCO-ratios in table 1 spins and parities are established up to top of the bands. At the bottom of band 8 it is, for example, possible to assign $I^\pi = 27/2^-$ to the 12374 keV level. This assignment is based on the quadrupole character of the transitions at 1254, 3042, and 3561 keV, which have $R_{\rm DCO}$(30-83) ratios of 1.01(11), 1.01(15), and 1.00(16), respectively. Alternatively, the 3678 keV transition, which connects the 11121 keV state in band 8 with the level at 7443 keV in structure 1c, has obviously stretched $\Delta I = 1$, mixed $E2/M1$ character due to its small $R_{\rm DCO}$(30-83) = 0.19(5) value. An estimate of the average quadrupole moment was not possible.

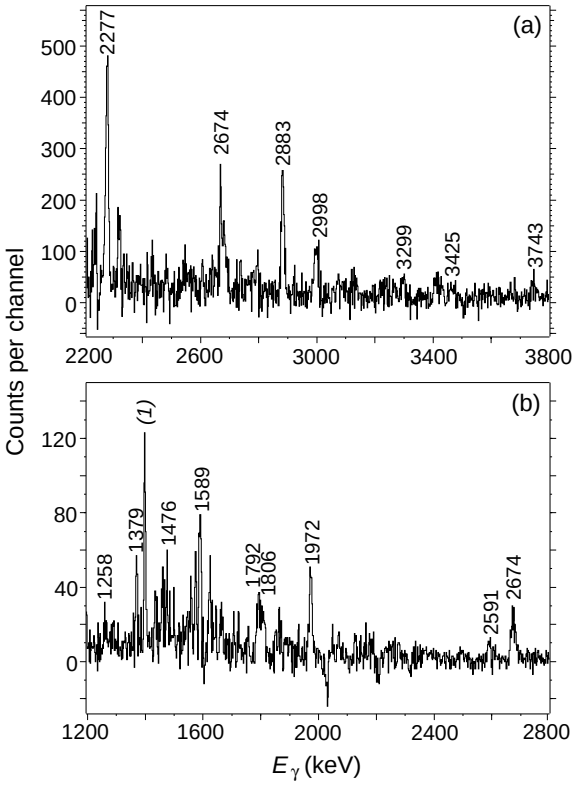

Fig. 16. Gamma-ray spectra related to structure 7. They were generated by summing gates on the transitions at 616 and 641 keV (panel (a)) and are measured in coincidence with the 4100 keV transition (panel (b)). See text and caption of fig. 6 for details.

3.8 Structures 9 and 10

Structure 9 is shown on the left-hand side in fig. 19. It is the only structure which could not be linked into the low-spin states. Therefore, the spins, parities, and excitation energies of the band have not been determined, and it has been placed at a reasonable but arbitrary spot in excitation energy ($X = 14$ MeV), which is mainly based on the relative intensities and energies of the band members.

The right-hand side of fig. 19 shows structure 10. The band reaches $I^\pi = (47/2^+)$ at an excitation energy $E_x = 25.7$ MeV. It decays exclusively into structure 1d, the topmost three levels of which can be seen in the middle of fig. 19. Parts of structure 10 are indeed visible in the γ-ray spectrum of fig. 6(b). The 1811 keV transition, which feeds the 13519 keV state of structure 1d has $R_{\rm DCO}$(30-83) = 0.67(7). This implies a spin $I = 31/2$ assignment to the 15330 keV level. Similarly, the $R_{\rm DCO}$(30-83) = 0.6(2) result of the 3110 keV transition suggests an $I = 27/2$ assignment to the state at 13479 keV. Since both DCO-ratios are compatible with a vanishing quadrupole admixture, positive parity is tentatively assigned to band 10, because at γ-ray energies of some 2-3 MeV a considerable $E2$ admixture should be present in $\Delta I = 1$ transitions (see, *e.g.*, the 3678 keV transition in structure 8). The 3050 keV transition has a $R_{\rm DCO}$(30-83) = 1.01(15) value, which provides the $I^\pi = 29/2^-$ assignment to the third

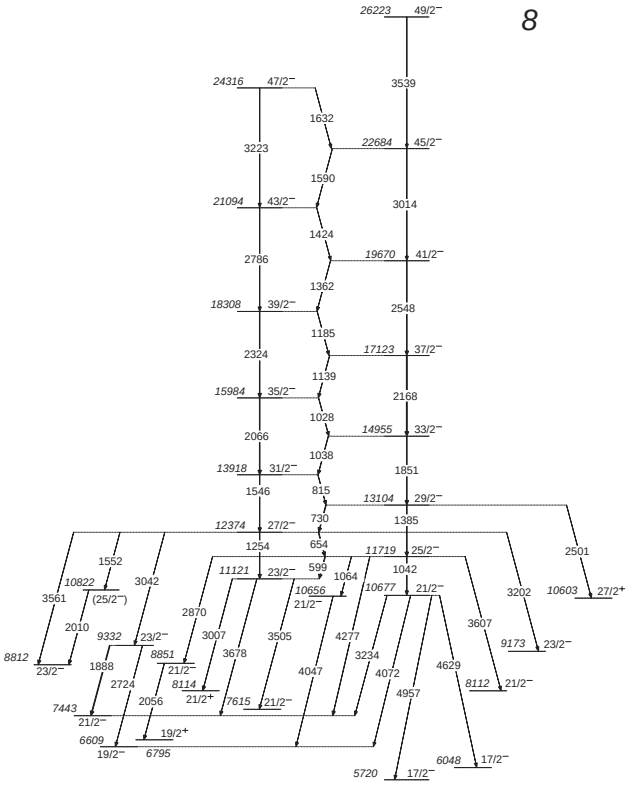

Fig. 17. Structure 8 of the level scheme of ^{59}Cu. See caption of fig. 5 for details.

level at some 13.5 MeV excitation energy. The 2276 and 2323 keV transitions in the band have DCO-ratios consistent with their quadrupole character, while the tentative spin assignments towards the top of the band are based on the regular rotational character.

4 Theoretical interpretation

4.1 Shell model calculation

The nucleus ^{59}Cu has only three particles outside the doubly magic ^{56}Ni core, two neutrons and one proton. This clearly calls for the spherical-shell model to try to interpret the low-spin states in ^{59}Cu, *i.e.*, structures 1 and 2. The shells involved near ^{56}Ni are the $1f_{7/2}$ shell below the $N, Z = 28$ shell gap, and the $2p_{3/2}$, $1f_{5/2}$, and $2p_{1/2}$ shells above the gap in the so-called upper fp shell. Another important shell is the unique-parity $1g_{9/2}$ intruder shell, which becomes essential for configuring the rotational bands in the mass region. However, it cannot be incorporated in the shell model calculations presented here.

The calculations we performed only allow for a maximum of two-particle two-hole excitations across the $N, Z = 28$ shell gap. The reason is a limitation in the dimension space, which can be accommodated with the RITSSCHIL shell model code [27] used in the calculations. The largest dimension treated within the restricted configuration space is about 20000, but the degree of agreement between experiment and predictions shows that the present approach comprises the essential ingredients to explain not only the excitation energies of the states, but more importantly the electromagnetic decay properties of the states belonging to structure 1. Structure 2 has positive parity. Hence, it involves at least one particle in the $1g_{9/2}$ shell, and thus is outside the model space.

The parameters of the calculations are identical to those presented in ref. [17]. The FPD6 residual interaction [28] is used together with single-particle energies, which within 10 keV reproduce a number of experimentally observed states in ^{56,57}Ni and ^{57}Cu (see ref. [17] for details). In essence, the shell gap at $N, Z = 28$ needs to be reduced with respect to the parameters used in ref. [28], which introduces increased "collective" correlations between the $1f_{7/2}$ and the $2p_{3/2}$ and $1f_{5/2}$ shells, respectively. As an effect, ^{56}Ni turns out to be a rather soft doubly magic nucleus, because the predicted wave function of the 0^+ state comprises a closed-core partition of merely 55% [17]. This number is in nice agreement with, for example, much more elaborate calculations in the full fp or $fpg_{9/2}$ model space employing quantum Monte Carlo diagonalization (QMCD) methods [29,30]. To describe the electromagnetic properties, we used effective charges $e_\pi = 1 + \delta e_\pi = 1.33e$ and $e_\nu = 2\delta e_\pi = 0.67e$ [31, 32] and effective g-factors $g_{\rm eff} = 0.9 g_{\rm bare}$.

The results of the calculation are summarized in figs. 20 and 21 and in table 4. Figure 20 compares the predicted and observed level energies of structure 1. For the 22 states of the sequences 1a, 1b, 1c, and 1d the comparison yields a small mean level deviation (MLD) of 208 keV and a binding-energy shift (BES) of 11 keV. The latter has been added to all predicted levels in fig. 20. It should be noted that the association of calculated states with those experimentally observed is based rather on their electromagnetic decay properties than on their energies. Table 4 provides the corresponding comparison of branching ratios b and mixing ratios $\delta(E2/M1)$. The overall good agreement between predicted and observed branching ratios manifests itself in a mean branching deviation (MBD) [34] smaller than 0.1. For completeness, the lifetime predictions are also included in table 4.

The maximum spin which can be obtained by coupling two like nucleons in the upper fp shell is $4\hbar$, *i.e.*, for the 29th and 30th neutron in ^{59}Cu. In a simple picture, the states belonging to structure 1a can thus be formed by coupling the $\nu(fp)^2_{0,2,4}$ configurations to a proton in the $2p_{3/2}$ shell. Similarly, structure 1b can be obtained by moving the active proton into the $1f_{5/2}$ shell, leading to $\pi(1f_{5/2}) \otimes \nu(fp)^2$ configurations. The γ-ray energies between the 3041 keV $9/2^+$ and 5425 keV $17/2^+$ levels (1486, 899 keV) of structure 2 are very similar to the cascades of structures 1a (1398, 1188 keV) and 1b (1476, 1056 keV) as well as to the 0^+–2^+–4^+ sequence in the even-even neighbour ^{58}Ni (1454, 1005 keV) [25]. This suggests that structure 2, up to the $17/2^+$ state, is based on $\pi(1g_{9/2}) \otimes \nu(fp)^2$ components, while the topmost $19/2^+$ state can be explained by a fully aligned $\pi(1f_{5/2}) \otimes \nu(1f_{5/2}) \otimes \nu(1g_{9/2})$ configuration.

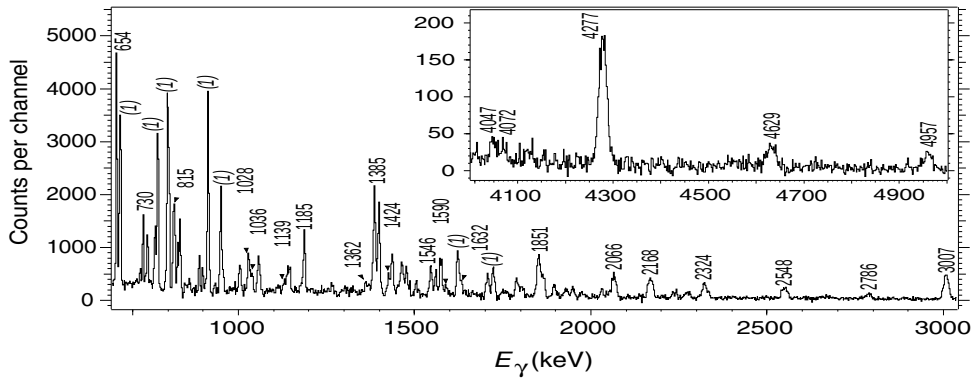

Fig. 18. Gamma-ray spectrum in coincidence with the 599 keV transition in structure 8. The inset shows the high-energy portion of the sum of γ-ray spectra in coincidence with transitions at at 1042 and 1385 keV. See text and caption of fig. 6 for details.

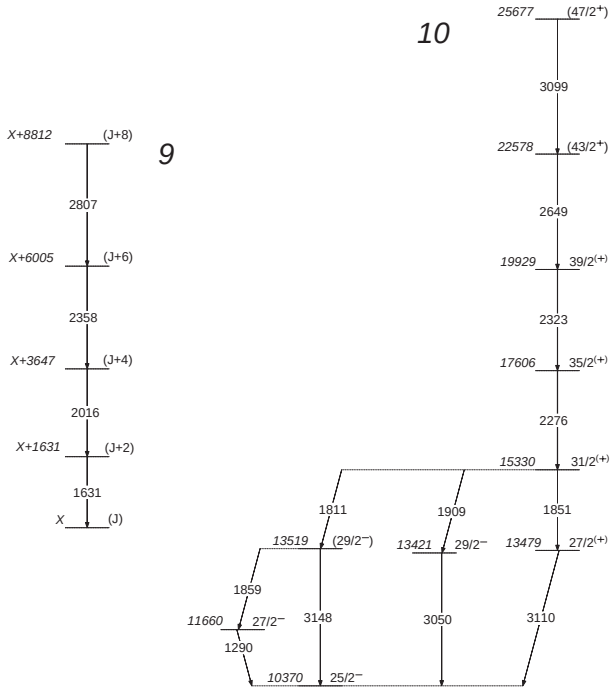

Fig. 19. Structures 9 and 10 of the level scheme of ^{59}Cu. See caption of fig. 5 for details.

This simple view of structures 1a and 1b is also reflected in the plot of the average occupation numbers in fig. 21(a) and (b). The softness of the ^{56}Ni core regarding particle-hole excitations manifests itself in the pronounced average value of 0.7–0.8 $1f_{7/2}$ holes for these two structures. Secondly, structure 1a is dominated by particles in the $2p_{3/2}$ shell, while structure 1b has larger contributions from the $1f_{5/2}$ shell. The $3/2^-$ ground state contains a 30% $\pi(2p_{3/2})$ closed-core partition, and the $5/2^-$ state at 914 keV is predicted to comprise only 20% of the respective $\pi(1f_{5/2})$ configuration. The filling of the $2p_{1/2}$ shell is basically identical in fig. 21(a) and (b), similar to the predictions for the number of $1f_{7/2}$ holes. The sudden rise in the $1f_{5/2}$ occupation at the highest possible spin for both structures, which happens on the cost of the $2p_{1/2}$ particles, is due to the fact that at least one neutron is needed in the $1f_{5/2}$ shell to create the $\nu(fp)^2_4$ configuration. The agreement between calculated and observed energies (cf. left-hand side of fig. 20) and decay properties (cf. table 4) of structures 1a and 1b are very good. The terminating character of the $11/2^-$ and $13/2^-$ states as well as the configuration change from the 914 keV $5/2^-$ state to the ground state is reflected by their comparatively large predicted lifetimes of some 5 ps.

Structure 1c has been interpreted as being built on a one-$1f_{7/2}$-hole configuration [24]. Possible spin values for such a configuration range from $7/2^-$ $[\pi(1f_{7/2})^{-1} \otimes \pi(fp)^2_0 \otimes \nu(fp)^2_0]$ to a maximum of $23/2^-$ $[\pi(1f_{7/2})^{-1} \otimes \pi(fp)^2_4 \otimes \nu(fp)^2_4$ or $\pi(1f_{5/2}) \otimes \nu(1f_{7/2})^{-1} \otimes \nu(fp)^3_{11/2}]$. In fact, the present extended observation of structure 1c in exactly this spin range supports the previous interpretation, which is further strengthened by the agreement between calculated and experiment level energies shown in the middle of fig. 20. The predicted branching ratios for decays within structure 1c also nicely match the observations, while slight deviations occur in the coupling of structure 1c with structures 1a and 1b, respectively. This can be attributed to the relatively small transitional matrix elements involved, which, for example, lead to a rather long calculated lifetime of $\tau = 95$ ps for the 1864 keV $7/2^-$ state. On the contrary, the lifetimes of the other states in the sequence are very short. This suggests the presence of modest collectivity already at relatively low spin in ^{59}Cu, which is further supported by the regularly increasing and nearly parallel behaviour of the occupation numbers of $1f_{7/2}$ holes and $2p_{3/2}$ particles in fig. 21(c). Towards the top of band 1c the average number of $1f_{7/2}$ holes reaches 1.8, *i.e.*, one more hole compared to structures 1a and 1b. Finally it is worth mentioning that the predicted and measured mixing ratios of the intense in-band $E2/M1$ $\Delta I = 1$ transitions are in perfect agreement (see table 4).

The states in structure 1d are interpreted as two-particle two-hole excitations across the $N = Z = 28$ gap. Since this excitation coincides with the limits of the present shell model calculation (see above) it is clear that the agreement cannot reach the level of the previously described structures in sequence 1. Nevertheless, it is possible to find a set of predicted states which are energetically in good

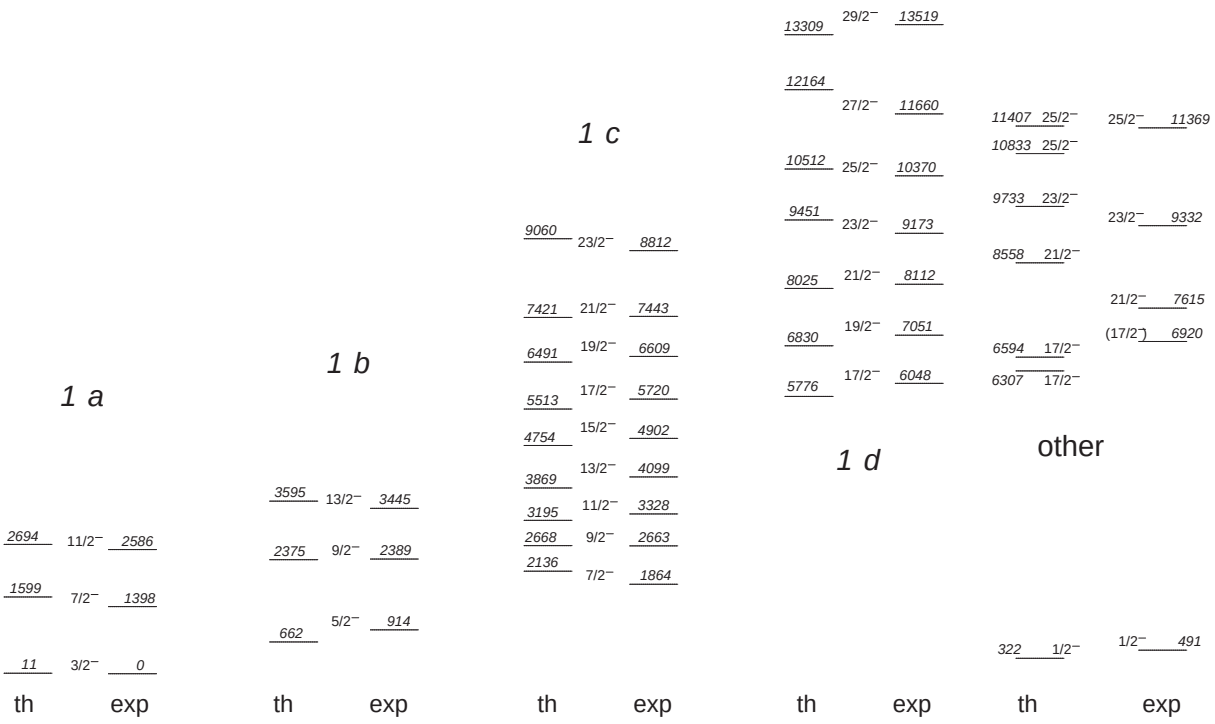

Fig. 20. Experimental excitation energies of structure 1 in ^{59}Cu are compared to results obtained from shell model calculations.

agreement with the experimental structure 1d. The decay characteristics of these states, namely the calculated first excited $17/2^-$, $19/2^-$, $21/2^-$, $23/2^-$, and $27/2^-$ levels together with the yrast $25/2^-$ and $29/2^-$ levels, match reasonably well the observed branching ratios. However, a clear band structure such as structure 1c does not develop in the calculations. Most likely, this is due to the necessary restriction of the model space, *i.e.*, the lack of additional particle-hole correlations on top of the primary particle-hole excitation. The former (mainly quadrupole) correlations relate to the average number of $1f_{7/2}$ holes of structures 1a, 1b (0.7–0.8), and 1c (1.3–1.8), respectively. The number of $1f_{7/2}$ holes of structure 1d is essentially 2.0 (see fig. 21(d)). The lack of the correlations may explain the suppressed in-band $E2$ strengths in structure 1d, *i.e.*, too small $\Delta I = 2$ branching ratios.

There are a few more negative-parity states observed in structure 1, which are shown on the right-hand side of fig. 20. In accordance with ref. [24], the $1/2^-$ level has a leading but small (22%) $2p_{1/2}$ single-particle configuration. The $(17/2^-)$ level at 6920 keV is relatively high in excitation energy. In fact, the calculated fourth and fifth $17/2^-$ states yield a dominant 3475 branch, but also additional and about equally strong transitions, which are not seen experimentally. A similar situation occurs for the 11369 keV $25/2^-$ state: A rather strong 38% branch connects the calculated third $25/2^-$ level to the yrast $21/2^-$ state, while two other relatively intense branches have not been seen. On the other hand, the experimental 7615 keV $21/2^-$ state is almost yrast, and there is a single predicted $21/2^-$ level nearby which could not even roughly match its characteristics. Note that the calculated yrast and first excited $21/2^-$ states are needed for structures 1c and 1d. Hence, it is natural to suggest a leading component of the wave function of the 7615 keV level, which lies outside the model space of the present shell model space, namely a fully stretched $[\pi(1g_{9/2}) \otimes \nu(1g_{9/2})]_{9^+} \otimes \nu(2p_{3/2})$ partition. The isospin $T = 0$ $[\pi(1g_{9/2}) \otimes \nu(1g_{9/2})]_{9^+}$ two-body matrix element is strongly binding. Similarly, we suggest a significant $[\pi(1g_{9/2}) \otimes \nu(1g_{9/2})]_{9^+} \otimes \nu(1f_{5/2})$ component in the wave function of the 9332 keV $23/2^-$ state.

4.2 Cranked Nilsson Strutinsky interpretation

The rotational states are interpreted in the framework of the configuration-dependent cranked Nilsson-Strutinsky (CNS) approach [35,36]. The advantage of this approach is that it allows to investigate many different bands in the calculations, because of its unique possibilities in specifying their configurations. The calculated single-proton orbits are shown in fig. 22 as a function of the rotational frequency $\hbar\omega$ for a constant deformation $\epsilon_2 = 0.27$, $\gamma = 20°$, and $\epsilon_4 = 0.0$. This is a typical mean deformation for the bands observed in ^{59}Cu. Included in fig. 22 are the $\mathcal{N} = 3$ high-j $1f_{7/2}$, low-j upper fp shell orbits, and the $\mathcal{N} = 4$ and $\mathcal{N} = 5$ high-j orbits $1g_{9/2}$ and $1h_{11/2}$. Due to its low-spin character and its unfavoured energetical position, the $2p_{1/2}$ subshell does not contribute significantly to the occupation of upper fp shell orbits at high spin, *i.e.*, in the following discussion the phrase "upper fp shell" refers basically to the orbits with $2p_{3/2}$ and $1f_{5/2}$ character. The black lines in fig. 22 represent orbits with signature $\alpha = +1/2$ and the grey lines represent orbits with signature $\alpha = -1/2$. Note the large signature splitting of

Table 4. Comparison of experimental branching and mixing ratios, b and δ, of γ-rays depopulating the negative-parity states in structure 1 with predictions from shell model calculations. The calculated lifetimes τ are provided as well.

E_x (keV)	I_i ($\hbar$)	I_f ($\hbar$)	E_γ^a (keV)	b_exp	b_theo	δ_exp^b	δ_theo	τ_theo (ps)
				Structure 1a				
1398	7/2	5/2	484	0.14(1)	0.35	+0.05(1); *+0.09(12)*	−0.03	0.80
		3/2	1398	0.86(1)	0.65			
2586	11/2	9/2	196	0.05(1)	0.08		-0.01	3.2
		7/2	*722*	n.o.	0.00			
		7/2	1188	0.95(1)	0.92			
				Structure 1b				
914	5/2	1/2	423	0.01(1)	0.01			6.1
		3/2	914	0.99(1)	0.99	$+0.24(^{11}_{7})$, $\sim +1.7$; *+0.29(3)*	+0.47	
2389	9/2	7/2	*525*	n.o.	0.00		−0.20	0.61
		7/2	991	0.11(1)	0.13	$+0.08(^{10}_{7})$	+0.26	
		5/2	1476	0.89(1)	0.87			
3445	13/2	11/2	*117*	n.o.	0.00		−0.03	3.9
		11/2	*782*	n.o.	0.00			
		9/2	860	0.16(2)	0.22	$+0.2 < \delta < +2.6$; $\sim$ *+1*	+0.27	
		9/2	1056	0.84(2)	0.78			
				Structure 1c				
1864	7/2	7/2	466	0.28(1)	0.08	$-1.19(^{24}_{29})$, $+0.07(^{10}_{11})$	−0.22	95
		5/2	951	0.48(2)	0.86	−0.02(5), $+4.1(^{11}_{9})$; *0.00(5)*	−0.11	
		3/2	1864	0.24(1)	0.06			
2663	9/2	9/2	*274*	n.o.	0.00		−0.02	0.38
		7/2	799	0.93(1)	1.00	−0.28(4); *−0.32(4)*	−0.28	
		7/2	1264	0.07(1)	0.00	$-0.48(^{12}_{13})$	−0.50	
		5/2	*1749*	n.o.	0.00			
3328	11/2	9/2	665	0.52(2)	0.72	$-0.15(^{5}_{4})$; *−0.09(5)*	−0.18	0.31
		11/2	742	0.14(1)	0.01	$-0.81(^{22}_{30})$	−0.07	
		9/2	939	0.02(1)	0.00		−8.00	
		7/2	1464	0.25(2)	0.25			
		7/2	1930	0.07(1)	0.02			
4099	13/2	13/2	654	0.06(1)	0.01		−0.04	0.17
		11/2	771	0.60(3)	0.67	−0.19(4); *−0.07(5)*	−0.18	
		9/2	1436	0.30(3)	0.20			
		11/2	1513	0.03(1)	0.12		−0.32	
		9/2	1710	0.01(1)	0.00			
4902	15/2	13/2	803	0.47(2)	0.63	$-0.18(^{6}_{5})$; *−0.31(6)*	−0.17	0.15
		13/2	1457	0.06(1)	0.02	$0.21(^{11}_{8})$	+0.02	
		11/2	1574	0.40(2)	0.35			
		11/2	2316	0.08(1)	0.01			
5720	17/2	15/2	818	0.40(2)	0.58	$-0.15(^{5}_{4})$	−0.16	0.16
		13/2	1622	0.51(2)	0.40			
		13/2	2276	0.09(1)	0.02			
6609	19/2	17/2	*561*	n.o.	0.03		+0.02	0.15
		17/2	888	0.41(2)	0.51	$-0.16(^{5}_{4})$	−0.20	
		15/2	1707	0.59(2)	0.47			
7443	21/2	19/2	*392*	n.o.	0.01		+0.00	0.16
		19/2	834	0.43(3)	0.52	$-0.20(^{6}_{5})$	−0.16	
		17/2	*1395*	n.o.	0.01			
		17/2	1723	0.57(3)	0.46			
8812	23/2	21/2	*700*	n.o.	0.01		+0.52	0.07
		21/2	1369	0.67(3)	0.61	−0.14(6)	−0.26	
		19/2	*1761*	n.o.	0.01			
		19/2	2204	0.33(3)	0.36			

Table 4. Continued.

E_x (keV)	I_i ($\hbar$)	I_f ($\hbar$)	E^a_γ (keV)	b_exp	b_theo	δ^b_exp	δ_theo	τ_theo (ps)
				Structure 1d				
6048	17/2	17/2	*328*	n.o.	0.02		+0.10	0.27
		15/2	*628*	n.o.	0.02		+0.38	
		15/2	1146	0.47(3)	0.58	$-4.1(^{8}_{16})$, $-0.32(6)$	−0.19	
		13/2	1949	0.43(3)	0.37			
		13/2	2605	0.10(2)	0.01			
7051	19/2	19/2	*442*	n.o.	0.04		+0.12	0.36
		17/2	1003	0.70(5)	0.15		−1.92	
		17/2	1331	0.16(3)	0.33	$-0.5 < \delta < +1.7$	+0.20	
		15/2	*1631*	n.o.	0.03			
		15/2	2150	0.14(3)	0.44			
8112	21/2	21/2	*669*	n.o.	0.04		+0.15	0.32
		19/2	1060	0.22(6)	0.18		−4.73	
		19/2	*1503*	n.o.	0.19		+0.58	
		17/2	2064	0.78(6)	0.56			
		17/2	*2392*	n.o.	0.00			
9173	23/2	23/2	*361*	n.o.	0.01		+0.06	0.07
		21/2	1061	0.19(8)	0.03		−4.67	
		21/2	1730	0.18(8)	0.68		−0.13	
		19/2	2121	0.63(13)	0.17			
		19/2	*2564*	n.o.	0.11			
10370	25/2	23/2	1198	0.13(4)	0.05		+0.37	0.04
		23/2	*1558*	n.o.	0.09		−1.09	
		21/2	2259	0.71(11)	0.06			
		21/2	2928	0.16(7)	0.79			
11660	27/2	25/2	*838*	n.o.	0.00		+0.36	0.19
		25/2	1290	0.17(7)	0.03		+0.98	
		23/2	2328	0.35(16)	0.73			
		23/2	2486	0.48(21)	0.16			
		23/2	*2848*	n.o.	0.07			
13519	29/2	27/2	*1408*	n.o.	0.01		−0.69	0.03
		27/2	1859	0.31(15)	0.11		−0.77	
		25/2	*2697*	n.o.	0.10			
		25/2	3148	0.69(15)	0.71			

[a] Italic numbers correspond to energetically possible but not observed (n.o.) transitions.
[b] Tilted values originate from the latest mass $A = 59$ data evaluation [33]. Their signs have been swapped to match the phase convention [19].

the high-j $1g_{9/2}$ and $1h_{11/2}$ intruder orbits. At frequencies larger than 1 MeV pronounced shell gaps at particle numbers 29 and 30 occur in the Routhian diagram. On the left-hand side of fig. 22 the origin of the orbits at spherical shapes is indicated. Due to the small Coulomb effects at these particle numbers, the corresponding plot for neutrons is almost identical. Moreover, moderate changes in the deformation parameters do not alter the global behaviour of the Routhians. The calculations do not include paring. Thus they are presumed to be realistic only at relatively high spins. On the other hand, it is also possible to obtain a qualitative understanding of the low-spin states, as will be demonstrated below. For further details see, for example, refs. [36,37].

Using the classification scheme of fig. 22 for the proton (and neutron) orbits, a band configuration can be defined as

$$\pi(1f_{7/2})^{-p_1} \otimes \pi(1g_{9/2})^{p_2} \otimes \pi(fp)^{p_3} \otimes \nu(1f_{7/2})^{-n_1} \otimes \nu(1g_{9/2})^{n_2} \otimes \nu(fp)^{n_3}. \quad (4)$$

Here, p_1 (n_1) is the number of proton (neutron) holes in $1f_{7/2}$ orbits, while p_2 (n_2) denotes the number of $1g_{9/2}$ protons (neutrons). Since ^{59}Cu has one proton and two neutrons (three valence particles) with respect to the doubly magic ^{56}Ni core,

$$p_3 = 1 + p_1 - p_2\,; \qquad n_3 = 2 + n_1 - n_2\,. \quad (5)$$

Therefore, it is sufficient to label the configurations of the deformed bands as $[p_1p_2, n_1n_2]$. In specific cases it is also instructive to indicate the signature α for the different

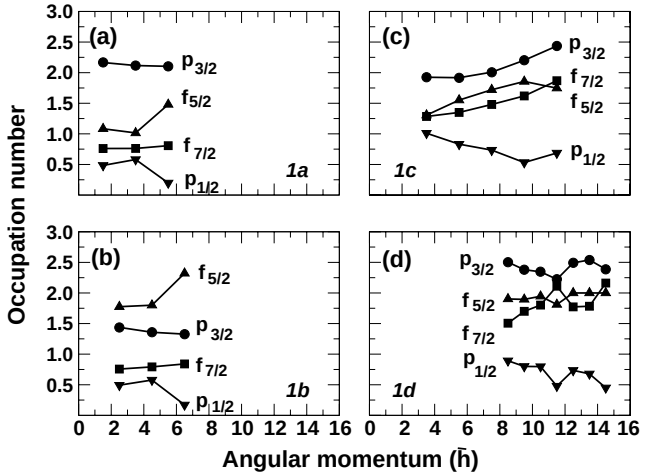

Fig. 21. Occupation number as a function of the angular momentum for the different sequences in structure 1. The squares represent the average number of holes in the $1f_{7/2}$ shell, while the circles and triangles correspond to the average number of particles in the $2p_{3/2}$, $1f_{5/2}$, and $2p_{1/2}$ shells, respectively.

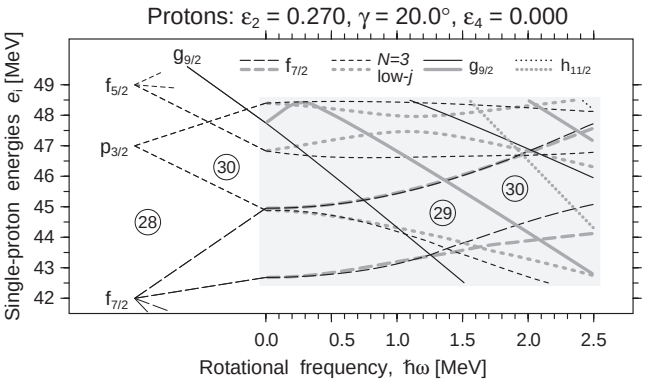

Fig. 22. Routhians calculated for protons at a typical mean deformation of ^{59}Cu.

subgroups. A more compact description would be $[q_1, q_2]$, with

$$q_1 = p_1 + n_1\,; \qquad q_2 = p_2 + n_2\,. \tag{6}$$

This labelling thus comprises several possibilities.

To facilitate the discussion, table 5 presents a number of possible configurations in matrix form. The rows are labeled with "$[p_1 p_2$" and with the maximum spin of the respective proton configuration. The columns are labeled with "$n_1 n_2]$" and the maximum spin values of the neutron configurations. The elements of the table are labelled with $[q_1, q_2]$, the number of combined proton- and neutron configurations, the maximum possible spin value of the configuration, and the index of the experimental band structure (italic style), which is assigned to a certain configuration. The number of bands is based on the product of the number of proton- and neutron subconfigurations for a given excitation. For example, the "10]" neutron subconfiguration involves four different structures due to the coupling scheme of the signatures of the single $1f_{7/2}$ hole and the third neutron in the upper fp shell, respectively. Except

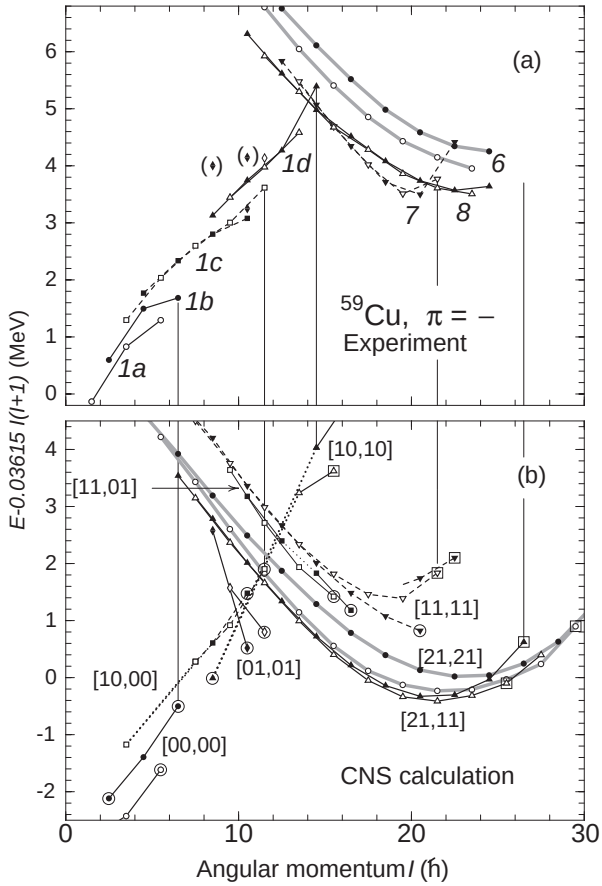

Fig. 23. Experimental (panel (a)) and calculated (panel (b)) energies of negative-parity states in ^{59}Cu relative to a rigid rotor reference. The experimental band are labelled with their identification number (cf. fig. 1), while the calculated bands are identified with their configuration (see text for details). Predicted band-terminating states are encircled, and states which correspond to the maximum possible spin for a given configuration (cf. 5) but are still collective are marked with a large open square. Some of these states are connected to the respective experimental band to ease the reading of the figure. Filled (open) symbols denote positive (negative) signature.

for specific configurations considered when discussing the experimental bands 9 and 10, the unfavoured signature of the $1g_{9/2}$ intruder orbit has not been included, because of the rather large excitation energy (see fig. 22). A total of some 100 bands has been calculated. By and large, each observed, indexed structure appears to correspond to exactly one type of a $[q_1, q_2]$ configuration. In general, it is identified with the one calculated lowest in energy. In the following, this is going to be described in some detail for negative- and positive-parity bands.

4.2.1 Negative-parity states (0, 2, or 4 $1g_{9/2}$ nucleons)

The upper panel in fig. 23 represents the experimental energies relative to an $I(I+1)$ reference for the negative-parity states in ^{59}Cu, while the lower panel provides the

Table 5. Overview of investigated CNS configurations and the observed structured assigned to them. The configurations are labelled as defined in eqs. (4)-(6). The last proton and neutron configurations correspond to unfavoured signature among the $g_{9/2}$. See text for more details.

Configuration	ν	00]		01]		10]		11]		21]		22]		22_{++}]	
π	$I^{\pi}_{\max}$	4^+		$6^-, 7^-$		$7^+, 8^+, 8^+, 9^+$		$11^-, 12^-$		$15^-, 16^-$		18^+		17^+	
[00		[0,0]		[0,1]		[1,0]		[1,1]		[2,1]		[2,2]			
	$3/2^-$	$11/2^-$	1a	4 bands		8 bands		4 bands		4 bands		2 bands			
	$5/2^-$	$13/2^-$	1b	$19/2^+$	2	$23/2^-$		$29/2^+$	3	$37/2^+$		$41/2^-$			
[01		[0,1]		[0,2]		[1,1]		[1,2]		[2,2]		[2,3]			
	$9/2^+$	1 band		2 states		4 bands		2 bands		2 bands		1 band			
		$17/2^+$	2	$21/2^-, 23/2^-$	1	$27/2^+$		$33/2^-$		$41/2^-$		$45/2^+$			
[10		[1,0]		[1,1]		[2,0]		[2,1]		[3,1]		[3,2]			
	$13/2^-$	$21/2^-$	1c	4 bands		8 bands		4 bands		4 bands		2 bands			
	$15/2^-$	$23/2^-$	1c	$29/2^+$	3	$33/2^-$	1d	$39/2^+$	4	$47/2^+$		$51/2^-$			
[11		[1,1]		[1,2]		[2,1]		[2,2]		[3,2]		[3,3]			
	$17/2^+, 19/2^+$	4 bands		8 bands		16 bands		8 bands		8 bands		4 bands			
	$19/2^+, 21/2^+$	$29/2^+$	3	$35/2^-$		$39/2^+$		$45/2^-$	7	$53/2^-$		$57/2^+$			
[21		[2,1]		[2,2]		[3,1]		[3,2]		[4,2]		[4,3]		[4,3]	
	$29/2^+$	1 band		2 bands		4 bands		2 bands		2 bands		1 band		1 band	
		$39/2^+$		$43/2^-$		$47/2^+$		$53/2^-$	8	$61/2^-$	6	$65/2^+$	5	$63/2^+$	9,10
[21$_-$												[4,3]			
	$27/2^+$											1 band			
												$63/2^+$	9,10		

corresponding CNS calculations. Figures 23(a) and (b) have been normalized arbitrarily. Only relative energies are meaningful to be compared.

The low-lying structures are observed from spin $I = 3/2^-$ to $11/2^-$ (structure 1a) and its signature partner from $I = 5/2^-$ to $13/2^-$ (structure 1b). These structures are understood as being built on [00,00] configurations with maximum spin values of $11/2^-$ and $13/2^-$, respectively (see table 5). At small deformation, these are the lowest-energy states obtained when the $1f_{7/2}$ orbits below the $N = Z = 28$ shell gap are filled ($p_1 = n_1 = 0$), and the three valence particles are placed in the upper fp shell ($p_2 = n_2 = 0$, $p_3 = 1$, and $n_3 = 2$, see eq. (4)). This assignment is in line with the simple shell model picture mentioned earlier (see subsect. 4.1).

Structure 1c is built on a $7/2^-$ band head and extends to spin $23/2^-$. It corresponds to either a proton or neutron hole in the $1f_{7/2}$ orbit, *i.e.*, to [10,00] or [00,10] configurations, respectively. Since the former [10,00] configuration involves a symmetric occupation in the upper fp shell (two protons and two neutrons in identical orbits) it is favoured in energy relative to the [00,10] configuration. Therefore, the [10,00] bands with maximum spins $21/2^-$ and $23/2^-$ form the two signature partners associated with structure 1c. The band head is described as prolate at $\gamma = -120°$. The higher-spin states would then be described as being built from the $K = 7/2$ spin vector of the proton hole pointing along the symmetry axis and a perpendicular component of collective rotation. Such states cannot be described in the present one-dimensional cranking formalism. When the spin values become higher, however, the components of the spin vector along the rotation axis will dominate and the present formalism should be valid. Thus, the calculated $7/2^-$ state and the $15/2^-$, $17/2^-$, ..., $23/2^-$ states are shown in fig. 23 and a smooth interpolation between $I^{\pi} = 7/2^-$ and $I^{\pi} = (15/2^-, 17/2^-)$ is indicated by a dotted line.

The states of structure 1d are likely to involve [2,0] configurations. Because two signature degenerate partners are observed, the band must have an odd number of $f_{7/2}$ proton holes and/or $f_{7/2}$ neutron holes. Hence, the only possible configurations are of [10,10] character. Eight different bands can be formed depending on the signature of the [303]7/2 $1f_{7/2}$ proton and neutron holes, and the signature of the odd neutron in the upper fp shell. A low energy $K = 17/2$ band head is then formed with the odd particles in the π[303]7/2, ν[303]7/2, and ν[321]3/2 Nilsson orbits. As for band 1c it is impossible to describe spin states just above the $I = 17/2$ band head, while it should be possible to describe the states close to termination. Thus, a smooth interpolation is carried out between $I^{\pi} = 17/2^-$ and $I^{\pi} = (27/2^-, 29/2^-)$. This leads to a qualitative description of the observed band (see fig. 23). The band is observed up to $I^{\pi} = 29/2^-$, which is somewhat below the maximum possible spin for the two signatures at 31/2 and 33/2, respectively. However, no clear termination is calculated at these spin values.

Higher-spin states of negative parity are formed when two particles are excited to the lowest $1g_{9/2}$ orbit. Here, it is always energetically most favourable to excite one proton and one neutron, both with signature $\alpha = +1/2$ (see fig. 22). Such an excitation can be combined with zero, one, two, three, and four $1f_{7/2}$ holes. With zero holes, *i.e.*, [01,01] configurations, energetically very favoured termi-

nating states are calculated at spins $21/2^-$ and $23/2^-$, respectively. In fact, the lower-spin states of these bands are calculated at a higher excitation energy. The calculated $21/2^-$ and $23/2^-$ states are likely to correspond to the experimental levels at 7615 and 9332 keV in structure 1. They are included in fig. 23(a) as filled and open diamonds. It should be noted that this assignment is in nice agreement with the results of the shell model calculations in sect. 4.1, which *cannot* describe these two specific states due to their $1g_{9/2}$ contents.

The [1,2] configurations are found within the eight [11,01] and two [01,11] configurations. They are calculated approximatively 1 MeV above yrast around termination at their maximum spin values of 33/2 and 35/2, respectively, and at even higher relative excitation energy for lower-spin values. The high energy calculated for these [1,2] configurations is in line with the fact that no experimental structures can be assigned to them.

Band 7 is interpreted as having two $1f_{7/2}$ holes and thus to be of type [2,2]. Because signature degenerate partners are seen, we conclude that there has to be one proton hole and one neutron hole, *i.e.*, the [11,11] configuration is favoured *versus* [21,01] or [01,21] candidates. As mentioned earlier, [2,2] configurations with two protons or two neutrons in the $1g_{9/2}$ orbit (for example, [12,10], [10,12], or [00,22]) are not considered either, because the large signature splitting of the [440]1/2 orbit leads to a rather high excitation energy of such configurations. The maximum spin values of the predicted yrast [11,11] configurations are $41/2^-$ and $43/2^-$. The observed topmost $45/2^-$ state of structure 7 might belong to the [11,11] band, which has the observed maximum spin value $45/2^-$. The calculated highest-spin states of this band are also shown in fig. 23(b). Another possibility is that the band is seen beyond its maximum-spin state because the $\alpha = 1/2$ branch does not terminate in a non-collective state at $I^\pi = 41/2^-$, but can rather be followed to even higher-spin states, which are formed because of the coupling between all $\mathcal{N} = 3$ subshells and between different major shells at very large rotational frequencies.

Band 8 is suggested to be based on configurations of type [3,2], *i.e.*, to have three holes in the $1f_{7/2}$ shell, which implies that there are four particles in the upper fp orbits. The most symmetric [3,2] configuration is [21,11], and the two signature branches are formed depending on the signature of the $f_{7/2}$ neutron hole. In a similar way, the [11,21] configuration is also calculated relatively high in excitation energy. Thus, the configuration of this band is fully determined contrary to some of the other bands. Structure 8 is observed to two spin units below the predicted $I_{\max}$. Furthermore, the calculated bands can be followed to higher spin values as illustrated by the 55/2 state in fig. 23(b) (see previous paragraph).

Finally, band 6 can be interpreted as having four $f_{7/2}$ holes, *i.e.*, to have a [4,2] configuration, and thus of the type [21,21]. The full configuration reads $\pi(1f_{7/2})^{-2} \otimes \pi(fp)^2 \otimes \pi(1g_{9/2})^1 \otimes \nu(1f_{7/2})^{-2} \otimes \nu(fp)^3_{+,-} \otimes \nu(1g_{9/2})^1$. Therefore, the signature partner bands are formed depending on the signature of the third fp neutron. The calculated signature splitting is consistent with experiment, which is a strong argument in favour of the present assignment (see fig. 23). The maximum spin values are $I = 59/2$ and 61/2, which is considerably higher than the observation of the bands. As expected for this kind of configuration with several holes and a number of high-j particles, the bands do not turn non-collective at $I = I_{\max}$ (cf. sect. 5). It is interesting to note that the $\alpha = -1/2$ signature partner of structure 6 behaves almost identical to the so-called doubly magic deformed [21,21] band in the $N = Z$ neighbouring nucleus ^{58}Cu [3,21,38]. Thus, $E_\gamma(^{58}\mathrm{Cu}) \sim E_\gamma(^{59}\mathrm{Cu}) + 50$ keV from spin $I = 11^+(23/2^-)$ to 23^+ $(47/2^-)$, and moments of inertia and alignments of the two bands are very similar.

Considering the maximum spin values and the fact that bands 7 and 8 are essentially signature degenerate, while band 6 is not, our assignments to them appear well founded. However, the calculated relative energies are off by 0.5–1.0 MeV. This suggests that the spherical gap at particle number 28 should be increased by at least 0.5 MeV, because the three bands differ in their $1f_{7/2}$ hole content. This modification can be done by a change of the Nilsson parameters, which will only marginally affect the relative energies within the bands.

4.2.2 Positive-parity states (1 or 3 $1g_{9/2}$ nucleons)

The upper panel of fig. 24 shows the experimental excitation energies relative to a rigid rotor reference for the positive-parity states in ^{59}Cu. The lower panel represents the corresponding CNS calculations.

Structure 2 starts with a $9/2^+$ band head and reaches maximum spins of $17/2^+$ and $19/2^+$, respectively. It is suggested to have [0,1] type configurations, *i.e.*, either one proton or one neutron in the $1g_{9/2}$ orbit. The [01,00] configuration, which has the proton in the $1g_{9/2}$ orbit, comes lowest in the calculations. This is also the natural assignment for the $9/2^+$ band head. The $19/2^+$ state, however, can only be reached for the [00,01] configuration with the odd proton in $g_{9/2}$ and two neutrons in the fp orbitals.

Band 3 is built from [1,1]-type configurations, *i.e.*, [11,00], [10,01], [01,10], or [00,11]. The [01,10] bands are relatively high in excitation energy, because they involve three neutrons in the upper fp shells. On the contrary, the [11,00], [10,01], and [00,11] configurations are calculated at similar energies. For the sake of clarity, only bands of the configuration [11,00] are plotted in fig. 24(b), *i.e.*, a proton being excited from the [303]7/2 Nilsson orbit directly into the [440]1/2 Nilsson orbit. Those which are lowest in energy terminate at spin $25/2^+$ and $27/2^+$, respectively, while another [11,00] configuration reaches the highest possible spin, $I = 29/2$. The $29/2^+$, $31/2^+$ and $33/2^+$ states at 12808 keV, 13527 keV, and 14517 keV (see fig. 7) are observed relatively low in energy, but we have not found any natural assignment for them, and thus are not shown in fig. 24.

Two-particle two-hole excitations across the shell gap are suggested for the experimental structure 4, *i.e.*, configurations of the type [2,1]. Here, the possibilities include [21,00], [11,10], [10,11] or [00,21] excitations. Once again,

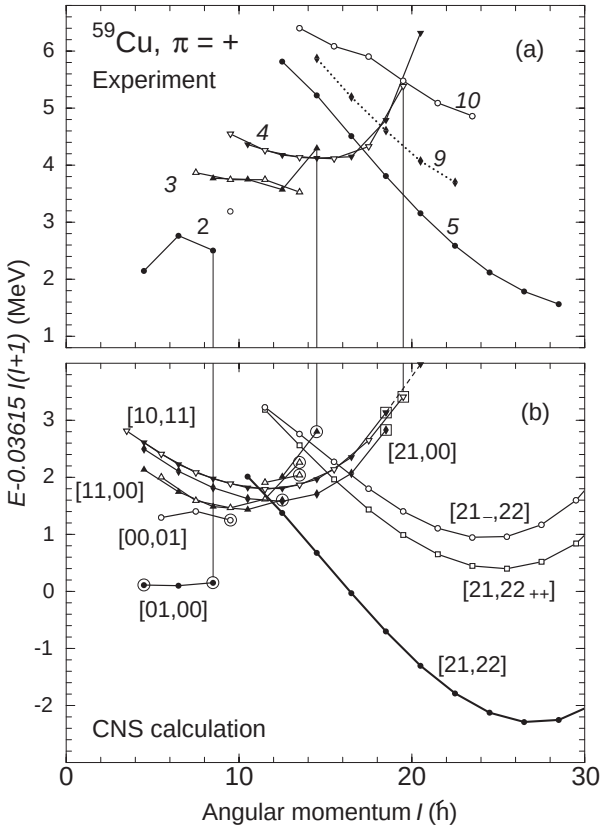

Fig. 24. Experimental (panel (a)) and calculated (panel (b)) energies of positive-parity states in ^{59}Cu relative to a rigid-rotor reference. See caption of fig. 23 and text for details.

the 16 [11,10] and 4 [00,21] configurations come relatively high in energy because of the three neutrons in the upper fp shell. The lowest calculated bands of the [2,1] type are [21,00] and [10,11], which is due to the symmetric occupation of the upper fp shell with both two protons and two neutrons. The [21,00] configuration is somewhat lower because with the present parameters the $g_{9/2}$ proton shell is rather lower than the neutron $g_{9/2}$ shell. However, because the observed structure 4 is signature degenerate with intense $\Delta I = 1$ transitions, it must have an odd number of $f_{7/2}$ holes for neutrons and/or for protons, because single particles or holes are needed in high-K Nilsson orbits (here: [303]7/2) to produce large $B(M1)$ values. This leaves the [10,11] configuration as the only alternative. These bands, which are calculated approximatively 300 keV above the [21,00] configuration, have very similar energies with $I_{\max} = 37/2$ and 39/2. They are somewhat collective at the $I_{\max}$ values although very soft towards the non-collective oblate shapes at $\gamma = 60°$. From this point of view it is questionable if they should be considered terminating or not. The remaining collectivity means that they can be followed continuously to higher spins. In the experimental level scheme a 41/2 state is seen on top of structure 4 (cf. fig. 9). Seemingly it belongs to the band, which implies that this configuration has been observed beyond $I_{\max}$. The calculated $41/2 \rightarrow 37/2$ transition energy is 3.7 MeV. This value is somewhat smaller than the observed energy difference of 4.4 MeV.

Structure 5 is the yrast superdeformed band in ^{59}Cu, to which a [4,3] configuration had been assigned previously [5]. In order to create energetically favoured high-spin positive-parity states in ^{59}Cu, it is clear that three particles must be excited to the $1g_{9/2}$ orbit. It is then possible to produce the very favoured [21,22] configuration, which is stabilized by the two large gaps at high rotational frequencies for particle numbers 29 and 30 in fig. 22. The lowest predicted [21,22] configuration is thus assigned to band 5, in accordance with the earlier publication [5]. Relative to the bands with one $1g_{9/2}$ particle and one or two $1f_{7/2}$ holes in their configuration, however, this band is calculated 1.5-2.0 MeV too low. This is consistent with the above-mentioned conclusion that the shell gap at particle number 28 is too small. It also suggests that the $1g_{9/2}$ orbit comes somewhat too low with the presently used standard Nilsson parameter set, which is contrary to previous conclusions in somewhat heavier nuclei (see, *e.g.*, ref. [38]). The maximum-spin state in this configuration is 65/2, but the band remains collective at this spin value and could in principle be followed to higher spins. It should be noted that the [21,22] is unique, because other possible [4,3] configurations, *e.g.*, [32,11] or [10,33], involve costly excitations both from well-bound [312]5/2 orbits and into high-lying [431]3/2 orbits.

Structure 10 can be understood as the signature partner of the yrast superdeformed band 5, which so far have not been seen in any other of the previously reported superdeformed bands in the mass $A \sim 60$ region. Interestingly, at the rather high excitation energy of this band, several possibilities arise to produce negative signature within the [21,22] scheme. First of all, there is the natural promotion of the single $1g_{9/2}$ proton from the favoured $\alpha = +1/2$ orbit into its $\alpha = -1/2$ signature partner, *i.e.*, the configuration labelled [21$_-$,22] in fig. 24(b). However, this configuration is calculated higher in energy than the configuration, which involves the excitation from the second into the third $1g_{9/2}$ neutron orbit. This corresponds to the [21,22$_{++}$] band in fig. 24(b), for which all three $1g_{9/2}$ particles are in $\alpha = +1/2$ orbitals. There are also other configurations at similar energies, *e.g.*, an excitation within the upper fp orbits starting from band 5, or with only three or two $1f_{7/2}$ holes combined with three $1g_{9/2}$ particles, *i.e.*, configurations of type [3,3] or [2,3]. Such configurations could also be possible assignments to structure 9, if it has positive parity. It should finally be added that the calculated yrast states of signature $\alpha = -1/2$ between $I = 51/2$ and 63/2 are formed with one proton excited from the $\mathcal{N} = 2$ shell to the $1g_{9/2}$ orbit relative to band 5.

5 Discussion

Twelve different structures have been observed up to high spin in ^{59}Cu. They involve different numbers of particle-hole excitations across the $N = Z = 28$ shell gap (q_1) and different numbers of particles in the $1g_{9/2}$ orbit (q_2). The latter orbit is strongly deformation driving. Together with an increasing number of particle-hole excitations, it is

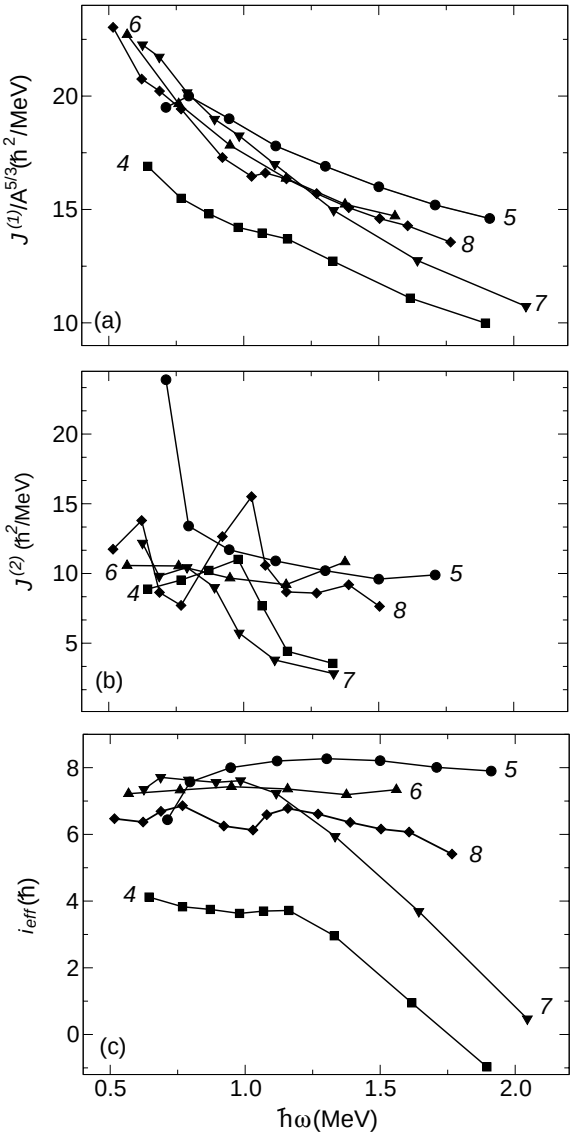

Fig. 25. (a) Experimental kinematic moments of inertia $J^{(1)}$, (b) experimental dynamic moments of inertia $J^{(2)}$, and (c) effective alignments i_{eff} *versus* rotational frequency for bands 4, 5, 6, 7, and 8. See text for details.

expected to induce an increasing amount of deformation or collectivity in the different structures. The extensive level scheme of ^{59}Cu thus offers an excellent and unique opportunity to study the evolution of shapes as a function of q_1 and q_2 or their sum $q = q_1 + q_2$.

In fig. 25(a) the kinematic moments of inertia of bands 4, 7, 8, 6, and 5 are plotted. They have configurations assigned to the classes [2,1] ($q = 3$), [2,2] ($q = 4$), [3,2] ($q = 5$), [4,2] ($q = 6$), and [4,3] ($q = 7$), respectively (see table 5 and subsect. 4.2). The evolution of shapes can be easily followed, because one would expect band 5 to have the largest deformation, and, therefore, also the largest moment of inertia, which it does have. Bands 6, 7, and 8 all have two $1g_{9/2}$ particles, and they also have rather similar values of their moments of inertia. At high spins and rotational frequencies ($\hbar\omega > 1.4$ MeV), the moments of inertia are also correlated with the number of holes in the $1f_{7/2}$ orbit. At low spins this correlation is probably destroyed because of pairing correlations or mixing with other members of the respective configuration class. Over the whole spin range band 4 has a considerably lower moment of inertia than the other bands, which is also expected since it only involves one $1g_{9/2}$ particle and the lowest q-value.

The comparison of dynamic moments of inertia $J^{(2)}$ in fig. 25(b) shows an essentially smooth behaviour for all the bands. There are some small irregularities visible for structures 4, 7, and 8, which support the above-mentioned idea of distortions of the yrast band of a given configuration by closely but energetically higher-lying bands of the same class. For band 4 and 7, the decrease of $J^{(2)}$ at high spins indicates the high energy required to achieve the last observed spin units, which are at or even beyond $I_{\max}$, the maximum spin which can be built from the available valence particles and holes.

In fig. 25(c) the experimental effective alignments i_{eff} of the bands 4, 5, 6, 7, and 8 are shown. The effective alignments i_{eff} measure the effect of additional particles with respect to an arbitrary ^{56}Ni core using the Harris parameters [39] $J_0 = 10\hbar^2/\mathrm{MeV}$ and $J_1 = 0$. The magnitude of the alignments of the bands is nicely correlated with the parameter q, *i.e.*, the number of $1g_{9/2}$-particles *and* the number of $1f_{7/2}$ holes involved in their configurations. The effective alignments of bands 4 and 7 decrease above $\hbar\omega \approx 1.1$ MeV indicating that they approach their termination.

A more precise measure of the deformation are the quadrupole moments of the bands. The average quadrupole moments, $\overline{Q}_{\mathrm{t}}$, of bands 4, 5, and 6 have been measured, and fig. 26(a) compares them to the calculated values as a function of the angular momentum. The calculations are based on the macroscopic density distribution as described in ref. [36]. The dot-dashed, dashed, and solid lines show the course of the CNS predictions, while the grey boxes reflect the experimental average values and their uncertainties within the measured spin range. For band 4 the dot-dot-dashed line shows the values used for the experimental attempt to describe a spin-dependent Q_{t} (cf. table 3 and fig. 4(a)). Qualitatively, this specific approach describes the data points, and it is in good agreement with the dot-dashed CNS prediction. Calculated shape trajectories of bands 4, 5, and 6 in the ϵ_2-γ deformation plane are shown in fig. 26(b). The bands change their shapes gradually starting near $\gamma = 0°$ prolate shapes, then they are calculated to be triaxial at intermediate spins, and they finally approach non-collective oblate $\gamma = 60°$ states at the highest spins. For band 6, which has the [21,21] configuration assignment, the shape trajectory is somewhat irregular. This is probably due to difficulties to discern between $1f_{7/2}$ and upper fp orbitals in the CNS calculations. Taking into account the deformation driving character of the $1g_{9/2}$ orbital, one can easily notice that the deformation of the bands increases depending on the number of the $1g_{9/2}$ particles involved in the their configurations: band 5 has the [4,3] configuration and it is more

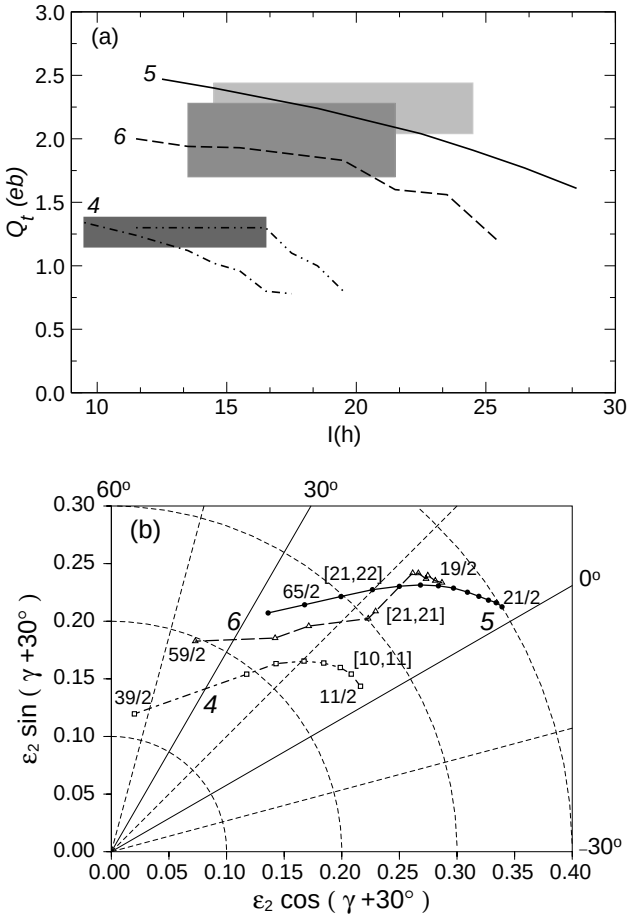

Fig. 26. Panel (a) provides a comparison of calculated and measured average quadrupole moments for structures 4, 5, and 6 (negative signature). The dot-dashed, dashed, and solid lines show the course of the predictions, while the grey boxes reflect the experimental average values and their uncertainties within the measured spin range. For band 4 the dot-dot-dashed line shows the values used for the attempt to describe a spin-dependent Q_t (cf. table 3 and fig. 4(a)). Panel (b) shows the calculated shape evolution of bands 4 (negative signature), 5, and 6 (negative signature) in the ϵ_2-γ deformation plane.

deformed than band 6, which belongs to the [4,2] configuration class, which is more deformed than band 4 with its [2,1] configuration.

The increase of the average quadrupole moments of bands 4, 5 and 6 is thus related to the $1g_{9/2}$ particle content involved in the band configuration. However, the importance of the $f_{7/2}$ holes, not only for the formation of smooth terminations, but also for their role in stabilizing the deformation has been emphasized [38,40]. Therefore, the $f_{7/2}$ holes are expected to have an important influence on the quadrupole moment. The contribution of the $1f_{7/2}$ holes and the $1g_{9/2}$ particles to the maximum spin is of similar size, because the full alignment of two $1g_{9/2}$ particles is 8 or 9$\hbar$, while the full alignment of two $1f_{7/2}$ holes is 6 or 7$\hbar$, depending on whether they are made of like nucleons (even spins) or unlike nucleons (odd spins). Correlating the gross $q = q_1 + q_2$ labelling and the measured average quadrupole moments for bands 4 (q = 3, [2,1] configuration, $\overline{Q}_t = 1.25(^{13}_{10})$ eb), 6 ($q = 6$, [4,2] configuration, $\overline{Q}_t = 1.95(^{33}_{25})$ eb), and 5 ($q = 7$, [4,3] configuration, $\overline{Q}_t = 2.23(^{27}_{22})$ eb), an empirical linear equation can be derived:

$$\overline{Q}_t \approx 0.53\,e\mathrm{b} + 0.24\,e\mathrm{b} \cdot q\,. \qquad (7)$$

This relation is also in line with quadrupole measurements in other $A \sim 60$ nuclei [1,3,4,6]. Assuming an axially symmetric shape, the corresponding quadrupole deformations β_2 for bands 4, 6, and 5 extracted from the transitional quadrupole moments are 0.24(2), 0.36(4) and 0.41(5), respectively [41]. This gives to an equation similar to eq. (7), namely

$$\varepsilon_2 \approx 0.09 + 0.04 \cdot q\,. \qquad (8)$$

The numbers are close to the ϵ_2-values at low spins (cf. fig. 26 and ref. [41]).

6 Conclusions

In the present work, a very extensive high-spin level scheme of ^{59}Cu is presented. Normalized to mass, the ^{59}Cu level scheme of fig. 1 is to our knowledge the most comprehensive high-spin level scheme ever deduced. Due to the combination of the very efficient γ-ray spectrometer Gammasphere and the selective device Microball a considerably amount of new experimental information has been extracted. Twelve structures representing more than 300 γ-ray transitions were placed in the ^{59}Cu level scheme. Each structure has been studied in detail both experimentally and theoretically. At low spin and low excitation energy simple restricted shell model calculations in the fp model space, which allow up to two particles to be excited across the shell gap at particle number $N = Z = 28$, successfully describe the excitation scheme, including branching and mixing ratios and a few lifetimes. At high spin and medium to high excitation energy it has been possible to follow the evolution of shapes from spherical to moderately-, well-, and superdeformed shapes along the level scheme by comparing the measured quantities to a large set of cranked Nilsson-Strutinsky calculations. A consistent configuration assignment has been performed, and a simple relation between the measured deformation and the summed number of particles in the $1g_{9/2}$ intruder orbit and holes in the $1f_{7/2}$ shell has been suggested.

Evidently, at this moment ^{59}Cu presents the most complete level scheme in the mass $A \sim 60$ region. A detailed study of the γ decay-out mechanism from the superdeformed bands and of the prompt proton decays is going to complete the present experimental work. Theoretically, ^{59}Cu offers the possibility to consistently refine the Nilsson parameters in the $A \sim 60$ region.

We would like to thank A.V. Afanasjev for valuable discussion and the accelerator staff at ANL for the excellent support. This research was supported by the Swedish Research Council, the Canadian NSERC, the U.S. Department of Energy under Contracts Nos. W-31-109-ENG-38 (ANL), DE-AC03-76SF00098 (LBNL), and DE-FG05-88ER40406 (WU), and the German BMBF.

References

1. C.E. Svensson *et al.*, Phys. Rev. Lett. **79**, 1233 (1997).
2. D. Rudolph *et al.*, Phys. Rev. Lett. **82** 3763 (1999).
3. D. Rudolph *et al.*, Phys. Rev. Lett. **80**, 3018 (1998).
4. C.E. Svensson *et al.*, Phys. Rev. Lett. **82**, 3400 (1999).
5. C. Andreoiu *et al.*, Phys. Rev. C. **62**, 051301(R) (2000).
6. C.-H. Yu *et al.*, Phys. Rev. C. **60**, 031305 (1999).
7. C. Andreoiu *et al.*, in *Proceedings of the International Workshop Pingst 2000 - Selected Topics on $N = Z$ Nuclei, June 2000, Lund, Sweden*, edited by D. Rudolph, M. Hellström, (Bloms i Lund AB, 2000) p. 21.
8. C.E. Svensson *et al.*, Phys. Rev. Lett. **80**, 2558 (1998).
9. D. Rudolph *et al.*, Phys. Rev. Lett. **89**, 022501 (2002).
10. D. Rudolph *et al.*, Phys. Rev. Lett. **86**, 1450 (2001).
11. I.-Y. Lee, Nucl. Phys. A **520**, 641c (1990).
12. D.G. Sarantites *et al.*, Nucl. Instrum. Methods A **381**, 418 (1996).
13. M. Devlin *et al.*, Nucl. Instrum. Methods A **383**, 506 (1996).
14. C.E. Svensson *et al.*, Nucl. Instrum. Methods A **396**, 288 (1997).
15. D.C. Radford, Nucl. Instrum. Methods Phys. Res. A **386**, 297 (1995).
16. J. Theuerkauf, S. Esser, S. Krink, M. Luig, N. Nicolay, O. Stuch, H. Wolters, Program Tv, University of Cologne, unpublished.
17. D. Rudolph *et al.*, Eur. Phys. A **4**, 115 (1999).
18. K.S. Krane, R.M. Steffen, R.M. Wheeler, At. Data Nucl. Data Tables **11**, 351 (1973).
19. H.J. Rose, D.M. Brink, Rev. Mod. Phys. **39**, 306 (1967).
20. B. Cederwall *et al.*, Nucl. Instrum. Methods A **354**, 591 (1995).
21. D. Rudolph *et al.*, Phys. Rev. C. **63**, 021301(R) (2000).
22. L.C. Northcliffe, R.F. Schilling, Nucl. Data Tables **7**, 256 (1970).
23. J.C. Wells *et al.*, LINESHAPE: *A Computer Program for Doppler Broadened Lineshape Analysis*, ORNL Physics Division Prog. Rep. 30, 1991, No. ORNL-6689.
24. S. Juutinen, J. Hattula, M. Jääskeläinen, A. Virtanen, T. Lönnroth, Nucl. Phys. A **504**, 205 (1989).
25. S.M. Vincent *et al.*, Phys. Rev. C **60**, 064308 (1999).
26. C. Andreoiu *et al.*, submitted to Phys. Rev. Lett.
27. D. Zwarts, Phys. Comm. **38**, 365 (1985).
28. W.A. Richter, M.G. van der Merwe, R.E. Julies, B.A. Brown, Nucl. Phys. A **523** 325 (1991).
29. T. Otsuka, M. Honma, T. Mizusaki, Phys. Rev. Lett. **81**, 1588 (1998).
30. T. Mizusaki, T. Otsuka, Y. Utsuno, M. Honma, T. Sebe, Phys. Rev. C. **59**, R1846 (1999).
31. A.K. Dhar, K.H. Bhatt, Phys. Rev. C **16**, 792 (1977).
32. P. Raghavan, M. Senba, Z.Z. Ding, A. Lopez-Garcia, B.A. Brown, R.S. Raghavan, Phys. Rev. Lett. **54**, 2592 (1985).
33. C.M. Baglin, Nucl. Data Sheets **69**, 733 (1993).
34. D. Rudolph, K.P. Lieb, H. Grawe, Nucl. Phys. A **597**, 298 (1996).
35. T. Bengtsson, I. Ragnarsson, Nucl. Phys. A **436**, 14 (1985).
36. A.V. Afanasjev, D.B. Fossan, G.J. Lane, I. Ragnarsson, Phys. Rep. **322**, 1 (1999).
37. I. Ragnarsson, W.C. Ma, Acta Phys. Pol. B **32**, 2597 (2001).
38. A.V. Afanasjev, I. Ragnarsson, P. Ring, Phys. Rev. C **59**, 3166 (1999).
39. S.M. Harris, Phys. Rev. B **138**, 509 (1965).
40. I. Ragnarsson, Acta Phys. Pol. B **27**, 33 (1996).
41. K.E.G. Löbner, M. Vetter, V. Hönig, Nucl. Data Tables A **7**, 495 (1970).